

Effect of metabolites on protein adsorption to PEO films

by

Meng-Yi, Wang

A thesis submitted in partial fulfillment of the requirements for the degree of

Master of Science

in

Material Engineering

Department of Chemical and Materials Engineering
University of Alberta

© Meng-Yi, Wang, 2021

Abstract:

Protein adsorption is a serious issue that affects a wide range of biomaterial applications. Hydrophilic polymer coatings, such as zwitterion polymers and polyethylene oxide (PEO), can inhibit protein adsorption at the material-blood interface. In addition, PEO is widely viewed as a golden standard, though the mechanism is not fully defined. Hemodialysis is traditional solution to treat patients with chronic kidney disease (CKD); however, metabolites with protein-bound property are difficult to be removed by this method. Besides, effect of small molecules on polymer remains ignored and unexplored. We applied quartz crystal microbalance with dissipation (QCM-D) to monitor the surface modified by PEO when introducing small molecules into the system. Ellipsometer, X-ray photoelectron spectroscopy (XPS), water contact angle and liquid chromatography mass-spectrometry (LC-MS) are also used to explore the potential of PEO to store the small metabolites. The results of QCM-D work showed HSA adsorption on HO-PEO film was affected by small molecules. The introduction of IS may modify the PEO film to decrease albumin adsorption. MS work showed the PEO film adsorbs these. This may indicate that the PEO film adsorbs a large variety of metabolites, which may have a direct impact on how proteins adsorb.

Preface:

This thesis is an original work by Mengyi Wang. The data in Chapter 4.2.3 was collected by Nanofab in University of Alberta. The data in Chapter 4.2.4 was collected by The Metabolomics Innovation Centre (TMIC) in University of Alberta. Except for the data collection in Chapter 4.2.3 and Chapter 4.2.4, all the data analysis in Chapter 4 and other chapters in this thesis are my original work.

Part of the content in Chapter 4.2.4 has been published as an abstract, Adsorption of Metabolites to Polyethylene Oxide (PEO) Thin Film and Its Influence on Protein Adsorption, at 36th Annual Meeting of Canadian Biomaterials Society (2021) from May 13th to May 15th. I was responsible for the data collection, data analysis and the manuscript writing. Professor Larry D. Unsworth was the supervisory author and was involved with concept formation and manuscript composition.

Acknowledgement:

I would like to show the highest gratitude and respect to my supervisor, Dr. Larry D. Unsworth. With his consistent support and clear guidance, I can overcome the difficulties during pursuing the master's degree. It is his patience and encouragement helping me complete my experiments and finally arrive the end of this journey.

I would like to show gratitude to my labmates, PhD candidates, Shammy Raj and Shuhui li. Despite the difference between our projects, they always listen to my opinions about experiments and help me relaxing from my work. It is their humor and advice accompanying me during the whole program.

I would also like to thank the other group members, Dr. Markian Bahniuk and Dr. Mehdi Ghaffari Sharaf. They help me being familiar with our lab and the campus. It is their suggestions letting me accomplish my research smoothly.

Last but not the least, I would like to thank my family. With their help and care, I can finish the experiments without worries.

Table of contents

Abstract:.....	ii
Table of contents.....	v
List of Tables.....	viii
List of Figures	ix
1. Introduction:	1
2. Theory:	5
2.1 QCM-D.....	5
2.1.1 Basic operation principle:	6
2.1.2 Sauerbrey equation:.....	7
2.1.3 Energy dissipation measurement:	8
2.1.4 Small-load approximation (SLA):.....	8
2.2. X-ray photoelectron spectroscopy (XPS):.....	10
2.2.1 Basic principle of XPS:.....	10
2.2.2 Similar techniques:	11
2.3 Ellipsometer:.....	13
2.3.1 Effect of surfaces on polarized light:.....	13
2.3.2 Measurement principle of Ellipsometer:	15
2.4 Water contact angle Theory	16
3. Material and methods:	18
Hypothesis:	22
4. Results and Discussion:	23
4.1 Synthesis of thiolated polyethylene oxide (PEO):	23

4.2	Ideal surface formation:	25
4.2.1	Surface Coverage - Ellipsometer:.....	25
4.2.2	Effect of PEGylation on Contact Angle:.....	26
4.2.3	X-ray photoelectron spectroscopy (XPS):	27
4.2.4	Mass spectroscopy:	29
4.3	Protein adsorption results:	32
4.3.1	Dissipation of each experiment:.....	32
4.3.2	HSA adsorption on Bare gold and PEO film:	33
4.3.3	Indoxyl sulfate (IS) adsorption on bare gold surface:	36
4.3.4	HSA adsorption on IS modified PEO surface:.....	37
4.3.5	HSA adsorption on IS modified Hydroxyl end-group PEO film through HFF-QCM:	38
4.3.6	HSA adsorption after small molecules modified thin films:	39
4.3.7	Simple mechanism and conclusion:.....	40
5.	Conclusion:	43
6.	Future work:	43
	Reference:	45
	Appendices:	53
	i: PBS solution recipe	53
	ii: Washing protocol for QCM sensors and small chips	53
	iii: QCM-D experiment	53
	Sweep	53
	Disturbance	54
	Detail of QCM experiment	56
	iv: Gold coating chips	57

v: Uremic toxin adsorption experiment on small chips 57

List of Tables

Table 4.2.1- 1 Ellipsometer results of PEO-modified surface and bare gold.....	25
Table 4.2.2- 1 Water contact angle of bare gold and thiol-PEO modified surface.....	27
Table 4.2.3- 1 Atomic composition of bare gold and PEO-modified surface.....	28
Table 4.2.4- 1 Different adsorption number of toxins by three solvents.	29
Table 4.2.4- 2 Three different adsorption tendencies during incubation with PBS extraction.....	30
Table 4.2.4- 3 Result of two different isomers extracted by PBS solvent.....	31
Table 4.3.1- 1 Dissipation data for experiments, average \pm SD (n \geq 3) at overtone = 3.	33
Table 4.3.2- 1 HSA protein adsorption on HO-PEO modified gold surface at overtone = 3.	33
Table 4.3.2- 2 HSA protein adsorption on CH3-PEO modified gold surface at overtone = 3.....	34
Table 4.3.2- 3 HSA adsorption on bare gold and PEO modified surface.....	36
Table 4.3.4- 1 Adsorption of IS and HSA protein two types of PEO film.....	38
Table 4.3.5- 1 HSA adsorption experiment with HFF-QCM.	38
Table 4.3.6- 1 Skatole and HSA adsorption on HO-PEO film at overtone = 3.....	40
Table 4.3.6- 2 Adsorption of skatole and HSA on two types of PEO film at overtone = 3.	40

List of Figures

Figure 1- 1The different modes of protein and small metabolites adsorption.	3
Figure 1- 2 Proposed mechanism of cell adhere on the PPR surface	4
Figure 2.1.1- 1 Operation principle of BluQCM.	6
Figure 2.1.2- 1 Description of QCM measurement.	8
Figure 2.1.4- 1 Viscoelastic media rheological spectra.	9
Figure 2.2.1- 1 Photoelectric effect.	11
Figure 2.2.2- 1 Auger analysis principle.	11
Figure 2.2.2- 2 Similar equipment to Auger.	12
Figure 2.2.2- 3 Example of XAS result.....	13
Figure 2.3.1- 1 Two polarized wave in light.	14
Figure 2.4- 1 Different contact angle measurements.	16
Figure 2.4- 2 Wenzel’s model.	17
Figure 2.4- 3 Cassie-Baxter model.....	17
Figure 2.4- 4 Hydrophilic example of Cassie-Baxter model.....	18
Figure 2.4- 5 Hydrophobic example of Cassie-Baxter model.....	18
Figure 3- 1 Experimental configuration of thiolation reaction.	19
Figure 3- 2 Experimental steps in LC-MS work.	20
Figure 4.1- 1 NMR result of mPEG.....	23
Figure 4.1- 2 NMR result of thiolated PEO.	24
Figure 4.2.3- 1. XPS result of bare and PEO modified Au.....	28
Figure 4.2.4- 1 The most concentrated toxins in complex solution.....	30
Figure 4.2.4- 2 The toxins with lowest concentration in the complex solution.	31
Figure 4.3.2- 1 Adsorption plot of HO-PEO and CH ₃ -PEO.....	35
Figure 4.3.2- 2 Adsorption of HO-PEO after overnight incubation.....	35
Figure 4.3.6- 1 Indoxyl sulfate and skatole.	39
Figure 4.3.6- 2 Water exclusions by skatole molecule.....	40
Figure 4.3.7- 1 Proposed mechanism of small molecules on PEO film.	42
Figure iii- 1 Sweeping result of the sensor.	54
Figure iii- 2 Disturbance signal in an experiment.	55
Figure iii- 3 The different disturbance signal reflected from different flowrate.....	56

1. Introduction:

Biofouling is a serious issue and causes problems in a host of industries from maritime vessels through to medical implants. Inert surfaces that resist the adsorption of molecules are considered vital to combatting biofouling. Despite 60+ years of research, no non-fouling surfaces have been identified. Protein adsorption remains the major barrier in the clinical adoption of materials as it is directly responsible for a host of deleterious effects like thrombosis and inflammation. Even though the adsorption of proteins has been studied at length, few have investigated the importance of the adsorption of small molecules that are commonly found in the blood, like metabolites. Thus, the effect of metabolites on non-fouling polymer films remains ill-defined.

The interaction of water at the material interface seems crucial to the success of low-fouling polymers. Polyethylene oxide (PEO) and polymers that incorporate zwitterions are two well-known hydrophilic polymers that resist protein adsorption at the solution-material interface. Zwitterion polymers imbue the surface with antifouling capabilities through the interactions with water and the zwitterion bond of the polymer [1, 2, 3]. Furthermore, protein adsorption and desorption may be affected through manipulating the charge of the film through altering solution pH. Despite the advantages of zwitterion polymers, their low reproducibility, pH sensitivity, surface density, and cost hinder their widespread adoption [3, 4]. In comparison, PEO is a hydrophilic polymer that is also hygroscopic *via* its high degree of hydrogen bonding. Compared to other low-fouling polymers, PEO has several inherent advantages, including having a tunable graft density and a low cost of production. Thus, PEO has attracted a lot of attention and is commonly considered the gold standard for low-fouling materials. The basic properties of PEO such as chemical structure [5], hydrogen bonding [6], growth mode [7], and stability [8] has been extensively studied. There are many papers that have investigated PEO's limits in inhibiting protein fouling under various conditions. These papers developed PEO as a versatile material such as PEO-involved copolymers [9-18], PEO as coating on nanoparticles [19-21], different conformations of PEO [22-24] and derivatives of PEO [25, 26]. Moreover, many have reported that PEO is a good additive to increase the antifouling ability of material [27-31].

Many mechanisms responsible for reduced protein adsorption have been postulated, including chain density, chain length and hydration state. Single-chain mean-field (SCMF) theory is used to explain the anti-fouling ability of short chain of PEO, which claimed chain density plays more significant role than chain length [32]. Monte Carlo et al. reported that helical chain can interact with water and, thus, lead to better resistance to protein adsorption [33]. Howorka and his team applied thermodynamics to explain the resistance [34]. Jiang and his team investigated linear and loop conformation of PEO and their relationship to antifouling ability on polydopamine surface [23]. Interestingly, loop conformation showed better protein resistance in the result. Jin et al. demonstrated that chain density has higher significance than chain length under the same conformation to fibrinogen adsorption [35]. Thromann's team suggested the conformation of PEG takes a key role to affect antifouling ability where transition from mushroom to brush can further enhance the protein resistance of the film [36]. Kingshott and his team also reported tuning chain density and the effect on cell adsorption [37]. Yang et al. demonstrated hydration state of different polymer and found water content plays an important role to protein resistance [38]. Unsworth et al. reported that distal group effect becomes significant when chain density beyond a critical value [39]. They claimed there is an optimal chain density for PEO film to resist protein adsorption [39-42]. Moreover, rearrangement of water on the surface and chain mobility were used to explain this idea [43].

Hydration is an important concept that scientists use to explain anti-fouling ability. A theory including disordered bulk water and oriented water at the interface of the surface explained that the repulsion between protein and layer is mainly due to mismatch of the hydrogen bond reported by Besseling et al [44]. This theory was then extended further by Whiteside et al. and concluded four properties that non-fouling layer owns: not hydrophobic, with hydrogen bond acceptors, without hydrogen bond donors, and electrically neutral [45]. In addition, Jia and his group reported the relation between many polymers and their non-fouling ability with water content [46]. They divided the water in polymer layer into two parts, inner part, and outer part, and suggested that water inside polymer layer may not affect protein adsorption for some polymers. Moreover, there is a negative correlation between water content and protein adsorption for PEG though the chain density is low and not enough to form brush on the surface. Furthermore, Yarovsky and his team reported that poly (2-oxazoline) (POX) may be the next

generation of anti-fouling polymer through computational simulation where the results showed short hydrophobic chains and long hydrophilic chains in a polymer can lead to competition between water and protein when they approach the surface. As a result of it, this kind of polymer has better non-fouling ability [26]. Though there are many exceptions, the above concepts provide strong background knowledge in this field for further anti-fouling ability investigation.

In contrast to hydration theory, there are few papers discussing about small molecules adsorption and their effect on the polymer layer [47, 48]. Prapainop et al. reported a new technique that nanoparticles modified by small metabolites can induce a folding event of protein which lead to better cell-specific result [49]. Chetwynd et al. reviewed papers about metabolite corona and suggested that fingerprint of metabolite corona may have similarity with protein corona fingerprint (Figure 1-1) [50]. Protein and metabolites can interact with each other and result in different type of adsorption mode on surfaces. Peter et al. reported two polymers ,poly (L-lysine)-graft-poly (ethylene glycol) (PLL-g-PEG) and PLL-g-PEG modified by Arg-Gly-AsP (RGD) (PLL-g-PEG-RGD), combined with small molecule, epigallocatechin-gallate (EGCg), and the effect of small molecule binding to cell adhesion and protein resistance [51]. The result showed cell adhesion induced by RGD is affected by adsorption of EGCg while the hydrogen bond formed between EGCg, and PEG also attribute to lower cell adhesion shown in Figure 1-2. All the above articles introduce an undeveloped and incredible idea that binding of small molecules may influence anti-fouling ability.

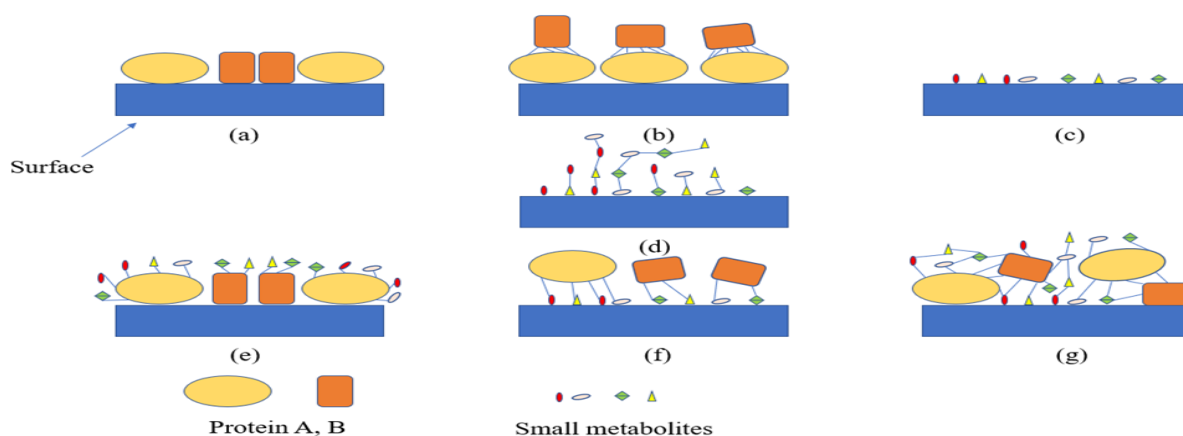


Figure 1- 1The different modes of protein and small metabolites adsorption [50]. a) Protein adsorption on bare surface b) Protein-protein interactions after protein adsorption on the surface

c) Small metabolites adsorb on the bare surface d) Metabolite-metabolite interactions after metabolites adsorption on the surface e) Protein-metabolite interactions after protein modified surface f) Protein-metabolite interactions after metabolite modified surface g) Complex interactions between proteins and metabolites.

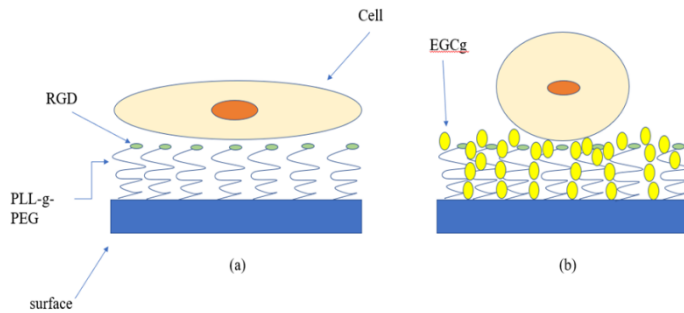


Figure 1- 2 Proposed mechanism of cell adhere on the PPR surface [51]. a) Cell can spread on the PPR surface by contact to RGD part b) The RGD segments are hindered, and the cell adhesion is affected and cannot spread out like a)

Chronic kidney disease (CKD) causes high mortality every year even with sophisticated modern medical systems. Uremic toxins accumulate in the blood of CKD patients. Based on their properties, uremic toxins can be divided into three groups, water soluble small molecules, middle molecules and protein-bound small molecules [52]. Because of the protein-bound property, the third type of uremic toxins are very difficult to remove using traditional membrane hemodialysis techniques. Indoxyl sulfate (IS) and p-cresol sulfate (PCS) are two well-known protein-bound uremic toxins. IS is the final product of tryptophan metabolism and is suggested to affect renal disease [53]. PCS can be traced to the metabolism of L-tyrosine or L-phenylalanine [54] and also contributes to renal diseases.

PEO is the gold standard of protein resistance material, however, it may lose its antifouling ability after being placed into complex milieu, such as milk and blood which largely hinders its medical applications. In addition, Leckband et al. reported that PEO may lose its resistance to protein adsorption under a certain condition [55, 56]. According to their conclusion, increased temperature can lower the energy barrier of protein adsorption on PEO layer. Moreover, PEO loses its protein resistance after breakdown of its conformation with force. Based on two-state theory, then the protein can attach on the inner part of PEO which is protein attractive part. This kind of conformation collapse can last for hours which highly depends on PEO molecular weight and temperature. On the other hand, most papers focused on the adsorption of macromolecules,

such as proteins, while few papers have been published on the effect of small molecules on PEO properties [49-51]. There are no papers detailing the interactions between small molecules and PEO thin films. It is our hypothesis that these small molecules may affect properties of polymer films leading to decrease or increase in their ability to resist fouling. To investigate this, we formed PEO thin films on gold surfaces. These PEO modified surfaces were incubated in solutions containing uremic toxins (individual or complex mixtures) which mimicked the blood of CKD patients. Toxin adsorption was evaluated using quartz crystal microbalance with dissipation (QCM-D) and Liquid chromatography-mass spectrometry (LC-MS). Furthermore, the effect of toxin adsorption to these PEO films on albumin adsorption was evaluated using QCM-D techniques as well. It is thought that understanding how small molecule adsorption occurs will provide further insight into how low-fouling films fail and spur the field to develop novel approaches that will yield truly non-fouling substrates.

2. Theory:

2.1 QCM-D

Quartz microbalance crystal with dissipation (QCM-D) was applied by many articles for analyzing the surface interaction [57-60]. QCM is an equipment based on piezoelectric principle, which can transfer the loading weight into signal with very high sensitivity, i.e., ng/cm². Dissipation is the energy loss per resonance which can offer the properties of the layer adsorb on the sensor. Because the samples for QCM-D do not need complicated processing and label to achieve high sensitivity, QCM-D are widely used in many fields, such as food industry. To further increase the sensitivity, high fundamental frequency QCM (HFF-QCM) was invented [61-63]. However, HFF-QCM sensors are very fragile and more complicated than low frequency QCM. The cost of it is also higher, thus HFF-QCM is not common as low frequency QCM. With QCM-D, researchers are able to explore extremely low mass adsorption, in our case, small toxin adsorption. In addition, it is able to monitor the film property difference after introduction of solution. Thus, QCM-D is usually combined with other equipment to achieve more comprehensive realize of the surface [64-66].

2.1.1 Basic operation principle:

QCM-D is based upon a piezoelectric design where changes in the resonance signal of a quartz crystal can be monitored as its mass changes. The resonance of the quartz crystal will be lower as increasing the mass based on Sauerbrey equation [57, 67]. The piezoelectric effect was found by a French scientist, René Just Haüy, which stated that a quartz begins to vibrate after being put into an AC electric field. As a standing wave, resonance of quartz can be excited to higher harmonics or overtones (eq. (2.1.1)). For measurement, the asymmetric motion of quartz is needed which limits the overtones to be odd, e.g., 1, 3, 5, 7... The equation below is used to describe the standing wave in QCM, where n is overtone, λ_0 is the wavelength or can be converted into fundamental frequency by $v = f \lambda$ and d is the thickness of sensor. From the equation, higher frequency is obtained as increasing overtone when d is constant:

$$\frac{n\lambda_0}{2} = d \dots \text{eq. (2.1.1)}$$

The measurement starts with comparison of the amplitude and phase voltage between the circuit that contains the crystal and a reference circuit of known impedance [68]. Then the voltages are represented by a complex equation (Figure 2.1.1-1 and eq. (2.1.2)):

$$Y(f) = G(f) + iB(f) \dots \text{eq. (2.1.2)}$$

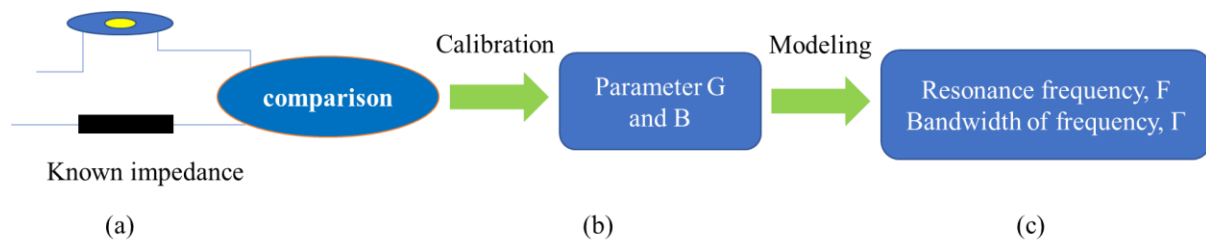


Figure 2.1.1- 1 Operation principle of BluQCM. (a) By comparison of circuit including known impedance and the circuit with QCM sensor, the result can be transferred into phase voltage and amplitude of voltage. (b) After calibration, the two parameters from comparison are converted to equation with parameter G and B. (c) Resonance frequency, F, and frequency bandwidth, Γ , are obtained after final modeling.

G is real number part in the fit while B is imagery part. F is the resonance frequency and Γ is related to dissipation. With this complex representation, the results can be fitted by another two equations and consequently provide frequency which is the measurement frequency, f [69]. And the bandwidth (Γ) of the frequency signal can be related to dissipation with the following equation:

$$D = \frac{2\Gamma}{f} \dots \text{eq. (2.1.3)}$$

D is dissipation and f is the frequency from the result of fitting equations.

2.1.2 Sauerbrey equation:

The Sauerbrey equation can be used to translate the QCM data. The frequency signal from QCM data can be converted into surface density by the following equation[59]:

$$\Delta f = -\frac{n}{C}m = -\frac{n}{C}\rho h \dots \text{eq. (2.1.4)}$$

$$C \propto \left(\frac{1}{f_0^2}\right) \dots \text{eq. (2.1.5)}$$

In which, Δf is the frequency difference between each stage of experiment, n represents overtones, C is the mass sensitivity constant, m is the adsorbed mass that can be divided into product of ρ and h which are adsorbed density and thickness, respectively. The mass sensitivity constant, C , only depends on fundamental frequency and the properties of the crystal.

The overtone of the crystal has only odd excitation numbers, that is 1, 3, 5, n , with different overtones, the fundamental frequency can be excited to higher frequency, i.e., $f_3 = 30$ MHz when $f_0 = 10$ MHz and $n = 3$. At higher overtones the penetration depth of the shear wave is smaller, in other words, the measurement will be closer to the middle of the crystal (Figure 2.1.2-1). At higher frequencies, the mass sensitivity increases (eq. (2.1.5)), where C is the sensitivity constant and f_0 is the fundamental frequency. [59, 70], it should be noted that data from different overtones are more important than just mass loading. With data from different overtones, the

adsorbed mass properties can be calculated when the adsorbed mass is not rigid. This also highlights a major limitation of the Sauerbrey equation, viz., it can only be applied to measurements in air or a rigid adsorbed mass because the viscosity of liquid can decrease the observed frequency.

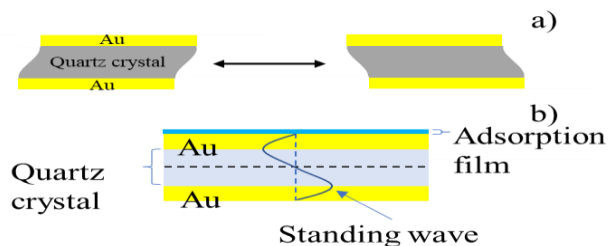


Figure 2.1.2- 1 Description of QCM measurement. a) Deformation of QCM sensor during resonance b) Standing wave propagating through the sensor

2.1.3 Energy dissipation measurement:

Dissipation can be very important in QCM-D work because it can offer properties of the adsorbed mass [58, 59]. When the acoustic shear wave penetrates the crystal, it inevitably decreases during the process. The simple concept is that if the media is rigid, the energy loss during the transportation will be smaller otherwise higher when the adsorbed mass is not rigid or it is thick enough. It is also important that overtones can be another mark for verification of the adsorbed mass properties, i.e., the frequency shift (Δf) from different overtones will be significantly distinct from each other when the adsorbed mass is not rigid. When the adsorbed film is thick enough or viscoelastic, Sauerbrey equation cannot be applied for the mass density and thickness measurement because of the imprecision of the frequency shift. With energy dissipation measurement, the failure of Sauerbrey equation of viscoelastic or thick adsorbed mass can be solved.

2.1.4 Small-load approximation (SLA):

When the adsorbed film is not rigid, the resulting adsorbed mass calculated using the Sauerbrey equation may be underestimated due to the acoustic wave being dampened in the viscoelastic

media [59]. Because of that, the data should be fitted with different models. Voigt-Kelvin model [71, 72] is the most common model that can be applied on viscoelastic film in QCM work. However, the model assumes that the real part of storage modulus, G' , is frequency-independent which only fits for some materials and gives a limitation of this model (Figure 2.1.4-1) [66].

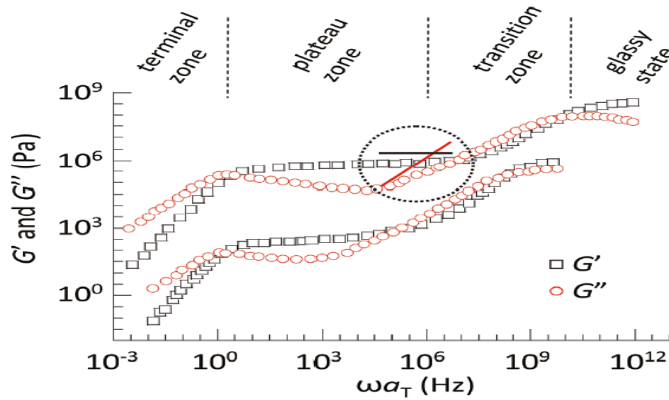


Figure 2.1.4- 1 Viscoelastic media rheological spectra. Relationship of storage modulus (G' , black line), loss modulus (G'' , red line) and product of angular frequency (ω) and temperature dependent factor (α_T) for long-chain linear polystyrene butadiene. [66]

The black line in the circle is the assumption from Voigt-Kelvin model, in which G' is an independent factor. Because of the assumption, data interpretation by Voigt-Kelvin model is only valid in this range. A model named ‘‘small-load approximation’’ is presented by Reviakine et al. [66] which involved measurable parameters from different overtones can give more precise adsorption amount and is shown below:

$$\Delta f_n \approx -\frac{n}{c} m_f \left(1 - n \omega_F \rho_l \eta_l \left(\frac{G_f''}{\rho_f (G_f'^2 + G_f''^2)} \right) \right) = -\frac{n}{c} m_f \left(1 - n \omega_F \rho_l \eta_l \left(\frac{J_f'}{\rho_f} \right) \right) \dots \text{eq. (2.1.6)}$$

$$\Delta \Gamma_n \approx \frac{n}{c} m_f n \omega_F \rho_l \eta_l \left(\frac{G_f'}{\rho_f (G_f'^2 + G_f''^2)} \right) = \frac{n}{c} m_f n \omega_F \rho_l \eta_l \left(\frac{J_f''}{\rho_f} \right) \dots \text{eq. (2.1.7)}$$

Where Δf_n and $\Delta \Gamma_n$ are the frequency shift and bandwidth difference of the frequency at n overtone, n is overtone and C is the mass sensitivity constant, m_f is the mass of the adsorbed film, and ρ_l and η_l are the density and viscosity of the liquid, respectively. ω_F is the angular fundamental resonance frequency and can be shown: $\omega_F = 2\pi f_F$ where f_F is the fundamental resonance frequency. G is the complex shear modulus which can be represented as $G = G' + iG''$ where G' is the real part and G'' is the imaginary part. $J = J' - iJ'' = G^{-1}$ where J' and J'' are the elastic and viscous components of the frequency-dependent compliance of the adsorbed film.

The equations above are too complicated and can be simplified as following when the penetration depth, $\delta = (2\eta_l / (2\pi n_f \rho_l))^{0.5}$ (in water at 5 MHz, at $n=1$, $\delta \approx 250$ nm), is thicker than the adsorbed film and the film is stiffer than the environment liquid [73]:

$$\frac{\Delta \Gamma_n}{f_n} = -\left(\frac{\rho_l}{\rho_f}\right) n \omega_F \eta_l J_F' \dots \text{eq. (2.1.8)}$$

From the above equation, it is easier to get J_F' and put it back to the original equations which can provide m_f , mass of the adsorbed film.

2.2. X-ray photoelectron spectroscopy (XPS):

2.2.1 Basic principle of XPS:

XPS is a common surface analysis technique developed for years [74] offering chemical composition information of the sample for research and industries [75]. The result of XPS shows peaks in a range of binding energy which can be converted into elemental information about the surface. This measurement is mainly based on Einstein photoelectric effect, which describes the electrons in elements can be excited by absorbing photons with specific energy level. The maximum analysis depth, 10 nm, is a big limitation for XPS. In addition, steady signal and contamination avoiding highly depends on vacuum extent, thus high vacuum is needed during measurement, though there is low vacuum XPS technology published recently [76]. The relation between photon energy and the binding energy can be presented with the following equation [77, 78]:

$$h\nu - E_k = E_b \dots \text{eq. (2.2.1)}$$

where the $h\nu$ is the energy of the photons and E_b is the binding energy of the element. Once the energy of photons is higher than the binding energy, the residual of the energy is transferred into kinetic energy, E_k . The photoelectric effect is shown as Figure 2.2.1-1.

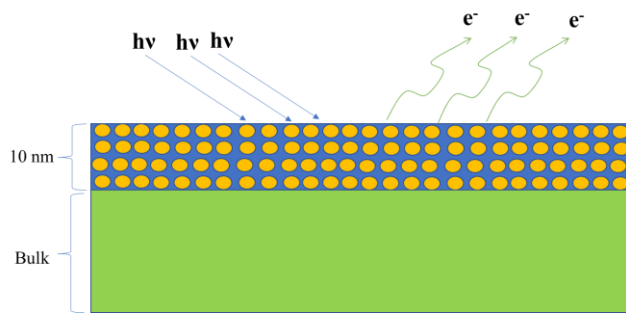


Figure 2.2.1- 1 Photoelectric effect. Electrons with kinetic energy (E_k) are emitted from the surface after the photons with enough energy are irradiated to the surface.

2.2.2 Similar techniques:

In XPS, x-ray is irradiated to the sample and then the photoelectrons are detected and measured. Besides of photoelectrons, auger electrons may also be generated during the process. When the electron is excited from the core level of the atom, the electron located at higher energy level falls down to fill the holes created by the excited electrons [79]. Because of the energy difference between these two electrons, another x-ray is emitted which may be absorbed by the third electron and excites it. The third electron ejected from the atom is named Auger electron, which can be transferred to surface information as well (Figure 2.2.2-1).

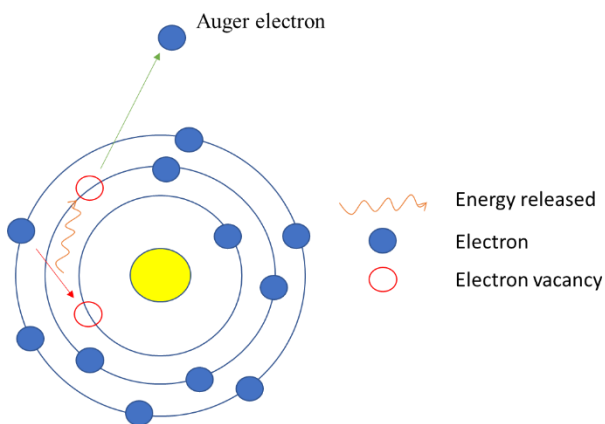


Figure 2.2.2- 1 Auger analysis principle. Auger electron is generated when the electron absorbs the energy released from the process that high-energy level electron falls back to fill the hole at low-energy level.

Instead of using x-ray, electron beam can be easily operated and focus, thus techniques using electron beam usually has higher intensity than XPS. Electron energy loss spectroscopy (EELS) and energy-dispersive x-ray (EDX) are two well-known measurement techniques. They are similar to XPS, need high vacuum to avoid contamination and steady signal while the difference is the sample using in EELS should be very thin for the electron beam to penetrate [80]. EELS is usually a compensated measurement equipment mounted in transmission electron microscopy (TEM). The electron beam loses energy by collision when penetrating and the loss energy can offer information of the sample. Different from EELS, EDX measures the x-ray emitted from high-energy level electron falling to the lower-energy core level hole [81]. In other words, except for EELS which needs penetration of electron beam, EDX and AES can happen when either electron beam or x-ray is irradiated to the surface (Figure 2.2.2-2).

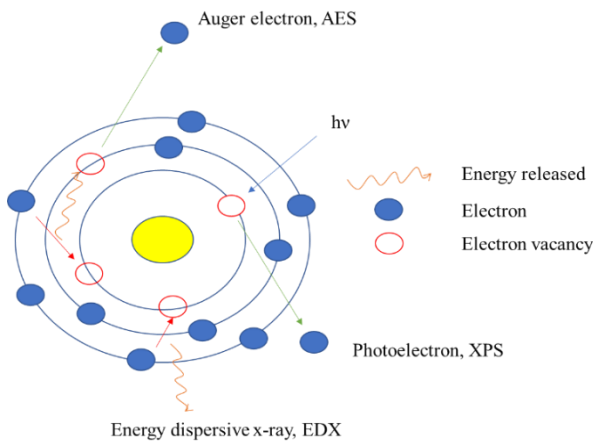


Figure 2.2.2- 2 Similar equipment to Auger. Summarize the relation of Auger electron, energy disperse x-ray and photoelectron and the corresponding measurement equipment. Photoelectron is ejected from atom after absorbing enough energy of photon. The hole produced from the photoelectric effect is filled by high-energy level electron and thus the energy between two electrons is released,

which is energy-dispersive x-ray. If energy-dispersive x-ray is absorbed by another electron and excites it, the final electron ejected from the atom is called Auger electron.

X-ray absorption spectroscopy (XAS) is another technique similar to XPS which also applies x-ray during measurement. XAS needs higher and intense energy, 2.0-20 keV, to see the absorption edge of the elements (Figure 2.2.2-3) [82]. The adsorption edge in XAS can be referred to the binding energy in XPS. Compared to XAS, XPS uses lower x-ray to excite electrons and is less sensitive.

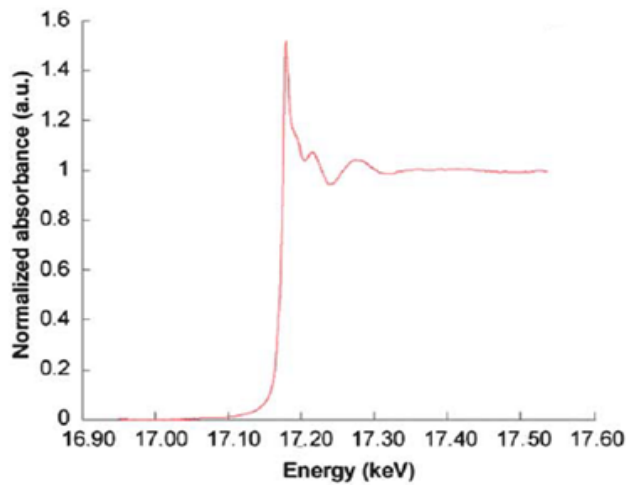


Figure 2.2.2- 3 Example of XAS result. The abrupt absorption signal is called as absorption edge which is unique to each element like binding energy in XPS [82].

2.3 Ellipsometer:

2.3.1 Effect of surfaces on polarized light:

An ellipsometer is optical equipment that can be used to measure the thickness and optical properties of thin films through light reflection or transmission at the surface. Reflection happens when light is emitted from a media to another media. A transparent media does not absorb light, and its refractive index is defined as n . On the other hand, most media are not transparent and absorb some part of light when light pass through, in this case, we use complex refractive index to describe its behavior when interacting with light [83, 84], $N \equiv n-ik$, where k is the extinction coefficient. When light is emitted into a different media, the speed of it will change as well as the angle between the incident light and normal line which can be described by Snell's law,

$$N_i \sin \theta_i = N_t \sin \theta_t \dots \text{eq. (2.3.1)}$$

where N_i and N_t are the complex refractive index of incident media and transmission media, respectively. θ_i and θ_t are the angle of incident or transmission light. Light emission can be divided into p- and s- polarized which differ from their oscillation direction in electric field (Figure 2.3.1-1). When light is irradiated to the sample and constructive or destructive

interference may happen due to different phase and amplitude change of p- and s- polarization upon reflection.

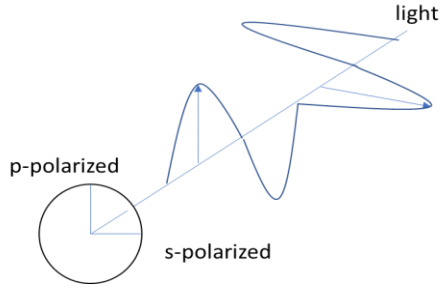


Figure 2.3.1- 1 Two polarized wave in light. Incident light can be divided into two p- and s- polarization based on their oscillation direction.

Fresnel equations show the amplitude of transmission or reflection coefficients for each polarized wave in light,

$$r_p \equiv \frac{E_{rp}}{E_{ip}} = \frac{(n_t \cos \theta_i - n_i \cos \theta_t)}{(n_t \cos \theta_i + n_i \cos \theta_t)} \dots \text{eq. (2.3.2)}$$

$$r_s \equiv \frac{E_{rs}}{E_{is}} = \frac{(n_i \cos \theta_i - n_t \cos \theta_t)}{(n_i \cos \theta_i + n_t \cos \theta_t)} \dots \text{eq. (2.3.3)}$$

$$t_p \equiv \frac{E_{tp}}{E_{ip}} = \frac{(2n_i \cos \theta_i)}{(n_t \cos \theta_i + n_i \cos \theta_t)} \dots \text{eq. (2.3.4)}$$

$$t_s \equiv \frac{E_{ts}}{E_{is}} = \frac{(2n_i \cos \theta_i)}{(n_i \cos \theta_i + n_t \cos \theta_t)} \dots \text{eq. (2.3.5)}$$

where r_p , r_s , t_p and t_s are the amplitude reflection and transmission coefficient for p- and s- polarization respectively. E with subscripts are the electric field of each polarized of reflection or transmission while n is the refractive index of reflection or transmission media. And θ with subscript is the angle of incident angle or transmission angle.

2.3.2 Measurement principle of Ellipsometer:

The thickness and optical properties of layers can be obtained by difference between light reflection or transmission. The amplitude and phase of p- and s- polarizations are varied after light reflection which can be measured by ellipsometer for calculation. In ellipsometer system, amplitude ratio and phase difference are represented as ψ and Δ respectively, where ψ is related to refractive index n , while Δ is related to extinction coefficient k . Both ψ and Δ can be obtained from ellipsometer by applying Fresnel equations:

$$\rho \equiv \tan\psi e^{(i\Delta)} \equiv \frac{r_p}{r_s} \dots \text{eq. (2.3.6)}$$

The above equation can be used to light reflection for s- and p- polarization, while the below equation is used for transmission case.

$$\rho \equiv \tan\psi e^{(i\Delta)} \equiv \frac{t_p}{t_s} \dots \text{eq. (2.3.7)}$$

By introduction of the definition r_p and r_s , the equations above can be revised as following[83]:

$$\rho \equiv \tan\psi e^{(i\Delta)} \equiv \frac{r_p}{r_s} \equiv \frac{\left(\frac{E_{rp}}{E_{ip}}\right)}{\left(\frac{E_{rs}}{E_{is}}\right)} \dots \text{eq. (2.3.8)}$$

where $E_{ip} = E_{is}$, so

$$\rho \equiv \tan\psi e^{(i\Delta)} \equiv \left(\frac{E_{rp}}{E_{rs}}\right) \dots \text{eq. (2.3.9)}$$

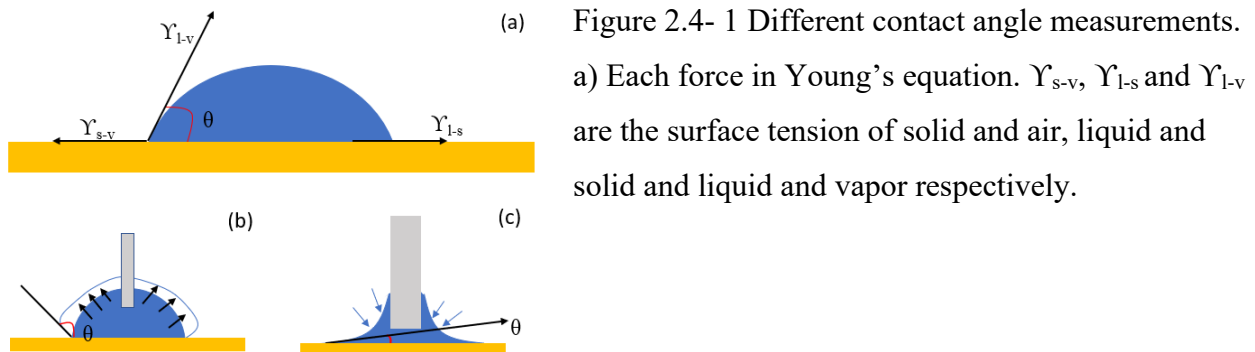
ψ and Δ vary largely with layer thickness and optical constants while ψ and Δ can be transferred into them through measurement of intensity of light reflection by simulation and calibration.

2.4 Water contact angle Theory

Surface properties play a significant role in antifouling materials. Water contact angles are a common and easy method to evaluate the surface energy. In short, contact angle is the angle of the water sphere on a surface. The smaller the angle is, the more hydrophilic the surface is. Young's equation is used to describe the relation between force on the surface. (Figure 2.4-1 a and eq. (2.4.1).).

$$\gamma_{l-v} \cos\theta = \gamma_{s-v} - \gamma_{l-s} \dots \text{eq. (2.4.1)}$$

Where θ is the contact angle. γ , γ' and γ'' are surface tension of liquid and vapor, vapor and solid and liquid and solid respectively. In addition to water contact angle, receding angle and advancing angle are also general methods to know the surface property. Receding angle is the angle between the water droplet and surface before the edge of water droplet decreases when the water droplet is pulled out (Figure 2.4-1 c). In comparison, advancing angle is the angle before the edge of water droplet extends when water droplet becomes bigger (Figure 2.4-1 b).



(a) Figure 2.4- 1 Different contact angle measurements.
 a) Each force in Young's equation. γ_{s-v} , γ_{l-s} and γ_{l-v} are the surface tension of solid and air, liquid and solid and liquid and vapor respectively.

The contact angle may be different when the surface is not flat and/or homogeneous. Wenzel's model and Cassie-Baxter model can be applied under this condition. There are three assumptions in Wenzel's model, the surface is rough but chemically homogeneous, local contact angle is given by Young's equation and the drop size is larger than the roughness. Based on these, the new contact angle given by Wenzel's model is shown in eq. (2.4.2) and Figure 2.4-2. Where r is a constant used to describe the calibrate the effect from roughness and θ is the local contact angle from Young's equation. And θ' is the new contact angle from Wenzel's model.

$$\cos\theta' = r\cos\theta \dots \text{eq. (2.4.2)}$$

$$r = A(\text{real})/A(\text{smooth}) \dots \text{eq. (2.4.3)}$$

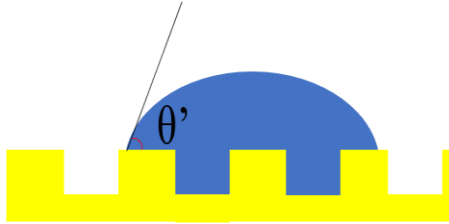


Figure 2.4- 2 Wenzel's model. The roughness increases the contact area between liquid and the surface. θ' is influenced by the roughness.

A is the area of rough surface or smooth surface. Compared with Wenzel's model, Cassie-Baxter model introduce chemically inhomogeneous to the surface which shown in eq. (2.4.4) and Figure 2.4-3.

$$\cos\theta'' = f'\cos\theta_y + f\cos\theta_g \dots \text{eq. (2.4.4)}$$

$$f' + f = 1 \dots \text{eq. (2.4.5)}$$

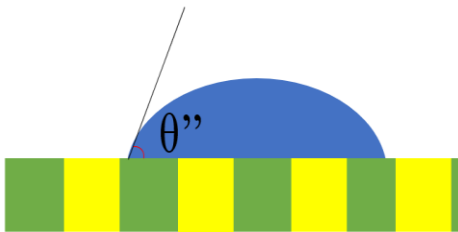


Figure 2.4- 3 Cassie-Baxter model. θ'' is influenced by chemical inhomogeneity on the surface.

Where f and f' are the fraction of each chemically different area. θ_g and θ_y are the contact angles of different chemical area. θ'' is the contact angle from Cassie-Baxter model. Bringing roughness to the system, there will be two different cases, one is hydrophilic surface and the other is hydrophobic surface. When the surface is hydrophilic, the equation is shown in eq. (2.4.6) and Figure 2.4-4.

$$\cos\theta'' = (1 - f) + f\cos\theta_g \dots \text{eq. (2.4.6)}$$

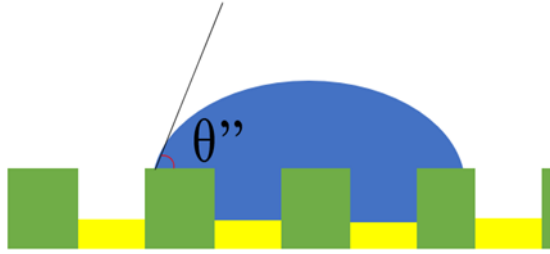


Figure 2.4- 4 Hydrophilic example of Cassie-Baxter model. Green and yellow regions represent different chemical compositions. Though the roughness part is filled by water, θ'' still increases.

Because the surface is hydrophilic, one contact angle is 0° which leads to $\cos \theta_y = 1$. The hydrophilic case of Cassie-Baxter model is very similar to Wenzel's model; however, it should be noticed that the new contact angle from Cassie-Baxter model will never become zero because f is not zero. For the hydrophobic case, the equation is shown in eq. (2.4.7) and Figure 2.4-5.

$$\cos \theta'' = -(1 - f) + f \cos \theta_g \dots \text{eq. (2.4.7)}$$

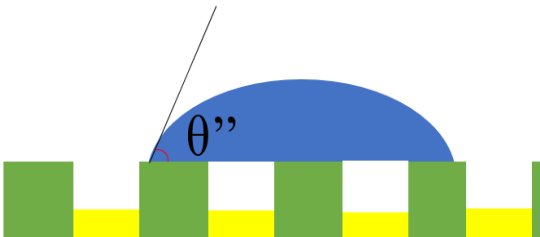


Figure 2.4- 5 Hydrophobic example of Cassie-Baxter model. Due to hydrophobic property of yellow area, air pocket exists in the roughness which make the contact angle elevate.

Due to the hydrophobic surface, the contact angle in the pocket is 180° which leads to $\cos \theta_y = -1$. From the above two cases, surface with inhomogeneity and roughness always becomes more hydrophobic.

3. Material and methods:

Thiolation of poly (ethylene glycol) monomethyl ether (mPEG) was synthesized thorough esterification. 30 ml toluene (Sigma-Aldrich, USA) as solvent was added into three-neck bottle where one side was stopped by glass stopper and a thermometer was fix at the other side for temperature monitoring (Figure 3-1). A reflux system filled with toluene was connected at the

middle of the three-neck bottle. Thus, the water from the esterification can be replaced by toluene and push the reaction forward to product side while the system was preheated to 85°C. 3 g mPEG was then added into the system and followed by addition of 0.37 ml mercaptoacetic acid (Sigma-Aldrich, USA). Three drops of sulfuric acid (Scientific Fisher, USA) were added into the system which then was heated to 110 °C in oil bath for 2 hrs. After the reacted product cooled down, the thiolated PEO was collected after precipitation in icy ether (Fisher scientific, USA) and dried in the oven overnight. The dried PEO product were then dissolved into 30 ml dichloromethane (DCM) (Sigma-aldrich, USA) and the solution was added into separatory funnel. Then 10 ml of 10% sodium bicarbonate, NaHCO₃ (Sigma-Aldrich, USA), solution was added into the funnel. The funnel was shaken to mix the two solution and stood still for 30 minutes to let the solution separated. The lower part of the solution was collected, and 20 ml DCM was added into the funnel to repeat the above steps three times. NaSO₄ (Sigma-Aldrich, USA) was added into the collected solution to remove water. The NaSO₄ solid was removed by filter and the solution was then transferred into rotary evaporator to get rid of most of the DCM for 30 minutes. The thiolated-PEO was collected by filter after adding icy ether into the rest of the solution. The product was dried in the oven overnight and characterized with NMR by dissolving in chloroform-d (Sigma-Aldrich, USA).

Thiol-terminated PEO-OH was purchase from Biochempeg Scientific Inc (USA). Both types of PEO solution were prepared at 5 mM with phosphate-buffered saline (PBS). IS and human serum albumin (HSA) were purchased from Sigma-Aldrich (USA) and their solution were prepared at 0.0445 mg/ml and 0.25 mg/ml in PBS, respectively.

Double-sided polished Si wafer (UniversityWafer, Inc., USA) coated with a 6 nm Cr adhesive layer and a 6 nm Au layer on both sides was used in uremic mass spectroscopy work. The wafer was diced into 0.5 x 0.5 cm² small chips and cleaned with exposure of UV light for 5 min, immersion into base piranha solution (1:1:5 volume ratio of 30 % hydrogen peroxide (Sigma-Aldrich, USA), 30% ammonia hydroxide (Sigma-Aldrich, USA) and MilliQ water) at 75 °C for 5



Figure 3- 1 Experimental configuration of thiolation reaction.

min, rinsed with a mixture solution (1:1 volume ratio of ethanol (Scientific Fisher, USA) and MilliQ water), dried by inert gas flow and final exposure of UV light for 5 min. Water contact angle, ellipsometer and x-ray photoelectron spectroscopy were applied before and after thiolated-PEO modified on the surface to characterized the surface property change. The clean small chips were incubated in thiolated-PEO solution overnight to obtain a fully covered film and then transferred into PBS solution followed by sonicated for 3 min to get rid of unbound PEO molecules. After dried by inert gas, the chips were incubated in uremic toxin for three different time periods, 10, 30 and 60 min. Then the droplets on the surface were cautiously removed by slight touch between the edge of chips and the uremic toxin solution. The chips were incubated in pure methanol (Sigma-Aldrich, USA) overnight to release the toxin in the film. The chips were removed and the solutions were sent for LC-MS analysis. The volume of methanol for incubation should be controlled as close to the solution volume require of mass spectroscopy as possible to avoid diluting the concentration of toxins. The whole process of toxin incubation work is shown in Figure 3-2.

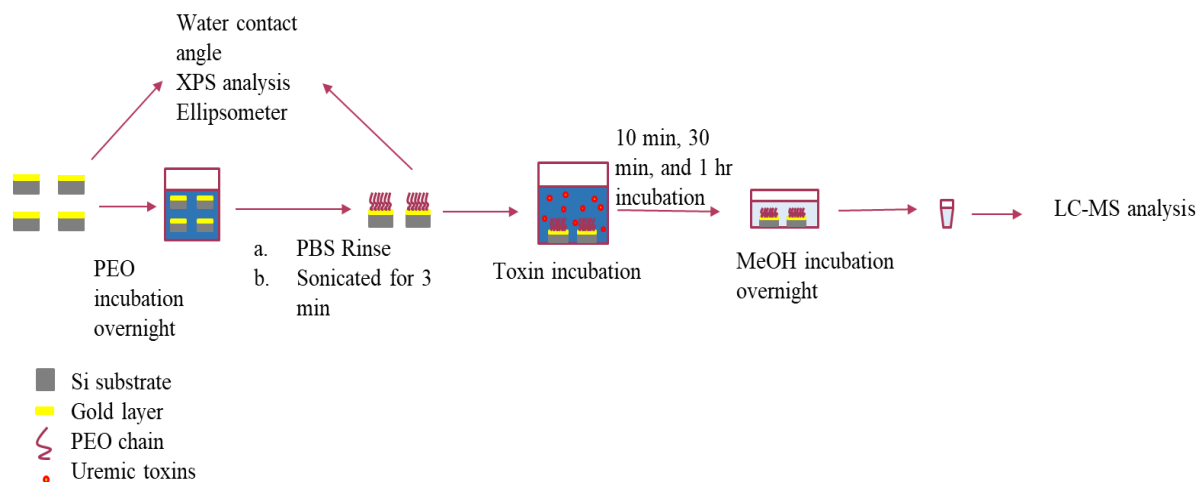


Figure 3- 2 Experimental steps in LC-MS work. Au chips were incubated in 5 mM PEO solution. After rinse, the chips were transferred into toxin solutions and incubated for 10, 30 and 60 minutes. The extraction of toxin was done by incubation in methanol overnight and the methanol solutions were then sent to LC-MS for analysis. T = 37 °C

BluQCM QSD (Biologic, France) was applied to monitor the interaction between HSA, IS and the PEO film. The AT-cut QCM-D sensors (Biologic, France) with fundamental frequency of 10

MHz were cleaned as the same protocol of small chips. QCM-D data was collected at 3rd overtone, temperature controlled at 37 ± 0.05 °C by and flowrate of 50 ul/min. PBS solution was injected for 1 hr to achieve baseline in frequency shift (Δf) and dissipation (ΔD). PEO solution was injected for 40 min followed by PBS rinse for 1hr. Then, IS solution was injected for 20 min followed by PBS rinse for 20 min. IS injection step can be skipped in the control group. HSA solution was injected for 20 min and the surface was rinsed with PBS rinse for 20 min. All the QCM-D results are shown at overtone = 3 in result and discussion part.

Hypothesis:

Polyethylene oxide has been proved to have anti-fouling ability for years. Despite there is no consistent agreement with the principle of its protein resistance, it is believed that chain density, chain length, distant group and hydration state play important roles, especially the chain density and hydration state. Though it is deemed as the golden standard to resist protein adsorption, PEO still fails when it is put into a relatively complex environment. In addition, there are few papers mention the interactions between small molecules and the non-fouling polymers, e.g., small metabolites, let alone to say the influence they cause in complicated milieu. My hypothesis is these small metabolites are the main reason causing PEO lose its protein resistance due to their adsorption may change the properties of the polymer film. For example, small molecules like sulfate ion with strong hydrated property may adsorb to the polymer and compete water molecules with the polymer lead to dehydration of the polymer. Thus, the hydration state of the polymer decreases as well as the rigidity of the film. Consequently, the polymer loses its non-fouling ability because of lower hydration state. The principal concept of this thesis is to investigate the effect of the small molecules adsorbed onto PEO film and which on protein adsorption.

4. Results and Discussion:

4.1 Synthesis of thiolated polyethylene oxide (PEO):

Polyethylene oxide was reacted with mercaptoacetic acid through esterification [85, 86] while the thiolated-PEO product was dissolved in chloroform-D and characterized using NMR (Figure 4.1-1). Meanwhile, virgin reactant, mPEG, was also characterized by NMR and compared with the product.

The characterization result of mPEG is shown in Figure 4.1-1. From the result, the singlet peak near 3.4 ppm is assigned to the methyl group at one end of mPEG (proton b). The triplet peak around 3.6 ppm is assigned to hydroxyl group at the other end of mPEG (proton c). The huge peak ranged from 3.6 to 3.8 is assigned to the main chain of the polymer, the ethylene oxide group (proton a).

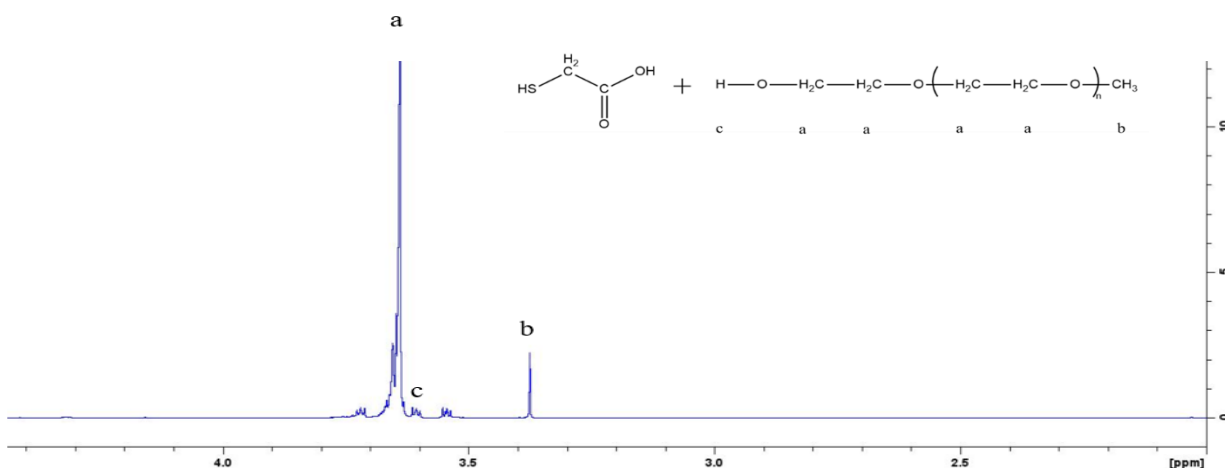


Figure 4.1- 1 NMR result of mPEG. Peak a is the main ethylene backbone. Peak b is the methyl group at the end of one side. Peak c is the hydroxyl group at the other end. Peak position is shown in Figure 4.1-1.

The characterization result of thiolated-PEO is shown in Figure 4.1-2 and its corresponding chemical formulae is shown in Figure 4.1-2. The peak at around 4.3 is the proton from methylene group which is in the ethylene oxide main chain and bonded to ester oxygen (proton

c). The peak ranged from 3.5 ~ 3.9 ppm indicates protons in the main chain of PEO (proton d). The singlet peak located at 3.4 is assigned to the methyl group at one end of PEO (proton e). Because the peak at 3.4 ppm also includes proton from unreacted PEO, its intensity can be a representative of product and unreacted reactant in the calculation of yield. The signal in the range of 3.3 ~ 3.4 ppm represents the protons from methyl group originally in mercaptoacetic acid (proton b) which is apparent and only present in the thiolated product and thus can be deemed as a sign whether the reaction is successful or not. The peak around 2 ppm is attributed from the proton in the thiol end-group from the other of the thiolated-PEO (proton a).

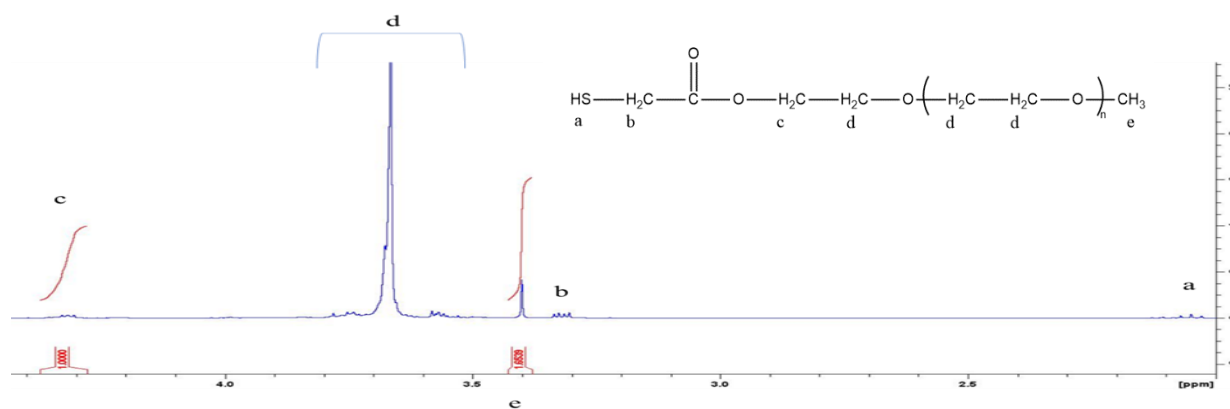


Figure 4.1- 2 NMR result of thiolated PEO. Peak a is the thiol group on one end. Peak b is the methylene group from mercaptoacetic acid. Peak c is methylene group near ester group. Peak d is the main backbone of PEO. Peak e is the methyl group on the other end. Peak position is shown in inset.

The yield ratio was obtained by the ratio between peak at 4.3 (proton c) and peak at 3.4 (proton e). The proton c signal represents the product and is divided by the proton e intensity which includes thiolated-PEO and unreacted PEO. It is noteworthy that the ratio should be divided by 2/3 when calculating the yield because signal of proton c is from two protons and signal of proton e is from three protons. The ratio was 1/1.65 in the characterization result and thus the yield is around 91%.

4.2 Ideal surface formation:

4.2.1 Surface Coverage - Ellipsometer:

Silicon wafers are used in mass spectroscopy work, and which are cleaned through piranha protocol to remove the surface contamination. Then the wafers are followed by chromium and gold coating with 6 nm thickness for each layer. After dicing into small chips (0.5x0.5 cm²), the surface of them is characterized by ellipsometer and contact angle to record the data for comparison with later PEO modified surface.

From Table 4.2.1-1, results of ellipsometer showed that the surface of small chips were coated with Cr and Au with thickness near 6 nm. In addition, thickness of PEO layer was also measured with Cauchy layer model where A, B and C were set as 1.45, 0.02 and 0.0 respectively. The simulation result of the PEO layer showed that the thickness was 3.22 nm with 0.65 nm as standard deviation.

Table 4.2.1- 1 Ellipsometer results of PEO-modified surface and bare gold. Data are present as average \pm SD (n \geq 4).

Sample	Cr	Au	PEO
Small chips	5.95 \pm 0.27	5.65 \pm 0.21	3.22 \pm 0.65

Moreover, with thickness of PEO layer, it can be used to calculate the chain density on the surface. There are two methods that can give the result of chain density, Lorentz-Lorentz relation [85] and the method Sofia reported [46].

Lorentz-Lorentz relation applied refractive index (n) which can also be measured by ellipsometer and the adsorbed amount per area (μ) was calculated as follow:

$$u = d\rho^o = \left(\frac{0.1M_w d}{A}\right)\left(\frac{n^2-1}{n^2+2}\right) \dots \text{eq. (4.3.1)}$$

where d and ρ^o are the thickness and density of the film respectively. M_w is the molecular weight and A is the molar refractivity of the PEO. A can be calculated from atom groups and molar

refractivity of atoms [87]. With the calculation result of μ , the chain density (σ) was obtained from the following equation:

$$\sigma = \frac{(N_a u 10^{-20})}{M_w} \dots \text{eq. (4.3.2)}$$

where N_a is the Avogadro's number, 6×10^{23} .

In contrast to Lorentz-Lorentz relation, Sofia equation applies average distance (L) between each chain instead of refractive index. The equation calculates distance between each chain, and which can be converted into chain density (σ):

$$L = \left(\frac{M_w}{\rho d N_a} \right)^{0.5} \dots \text{eq. (4.3.3)}$$

where M_w is the molecular weight and ρ is the density of the film while d is the thickness of the film and N_a is Avogadro's number. Molecular weight is 824 for the synthesized thiolated-PEO while density of the film is around 1.0 g/cm^2 and the thickness is measured by ellipsometer. With the information, the distance between each chain (L) can be calculated as 0.65. Then L is converted into chain density (σ) by the following equation:

$$\sigma = \frac{1}{L^2} \dots \text{eq. (4.3.4)}$$

With distance between each chain, the chain density can be calculated as 1.24 chain/nm^2 . This result proves that the PEO film on the small chips' surface are in the brush conformation while the mushroom conformation has lower chain density as 0.04 chain/nm^2 .

4.2.2 Effect of PEGylation on Contact Angle:

Contact angle can offer information about the surface, where a small contact angle represents higher hydrophilicity. The static and advancing contact angle of bare gold are both high, 72° and 63° , respectively, while the receding contact angle is smaller, 30.2° . After modification with end-tethered PEO the contact angle largely decreased from 72° to 40° and advancing angle decreased

from 63° to 46.8° while the receding angle decreased from 30.2° to 17.9°. Data from Table 4.2.2-1 shows that the Au surface were modified using thiolated-PEO.

Table 4.2.2- 1 Water contact angle of bare gold and thiol-PEO modified surface. Data are presented as average \pm SD (n \geq 6).

Surface	Contact angle	Advancing angle	Receding angle
Bare gold	72.02 \pm 7.25	63.0 \pm 2.2	30.2 \pm 2.2
Thiol-PEO-modified	39.95 \pm 6.64	46.8 \pm 5.2	17.9 \pm 3.3

4.2.3 X-ray photoelectron spectroscopy (XPS):

In addition to ellipsometer and contact angle, XPS was applied to analyzed to surface elemental composition. Moreover, the result was also used to compare the difference in elemental composition after thiolated-PEO modification. Furthermore, C1s high resolution scan on the surface was used to calculate the ratio of C-O bond and C-C bond which can further confirm PEO chemisorption because C-O bond is the main part in PEO. The results of XPS are summarized in Table 4.2.3-1.

From the result of scan of bare gold, gold has 53.7% elemental composition on the surface which is commonly found for bare gold. On the other hand, there were some contaminations indicated by oxygen and carbon components which may be contributed by the dust or atmosphere contaminants. Gold has 53.7% elemental composition on the surface which is reasonable for bare gold. By comparison with bare gold, results of thiolated-PEO showed gold component is decreased significantly after chemisorption from 53.7% to 11.8%. In contrast, carbon component and oxygen component are largely increased because oxygen and carbon are main atoms in PEO. Moreover, sulfur component also proves that the surface was modified by thiolated-PEO. The calculated C/O ratio is 1.9 and close to the theoretical value 2 which indicates the surface is covered by PEO film.

Table 4.2.3- 1 Atomic composition of bare gold and PEO-modified surface. Data are presented as average \pm SD ($n \geq 4$).

Surface	Au (84 eV)	C (285 eV)	O (532 eV)	S (162 eV)	C/O theory	C/O actual
Bare gold	53.7	35.0	11.3	Not detected	/	3.1
PEO-modified	11.8 ± 0.3	56.5 ± 0.1	30.2 ± 0.3	1.5 ± 0.1	2	1.9

From the C1s high resolution scan, the C-C component (285 eV) is measured as 75% and C-O component (286.5 eV) is much smaller than C-C component. In contrast, result of C1s high resolution scan after chemisorption showed that the component of C-O (286.5 eV) strongly increases from 25.4% to 59.1% while the component of C-C decreases much. In addition, contribution of C=O component (288.5 eV) also indicates the modification of PEO. The high-resolution results are shown in Figure 4.2.3-1.

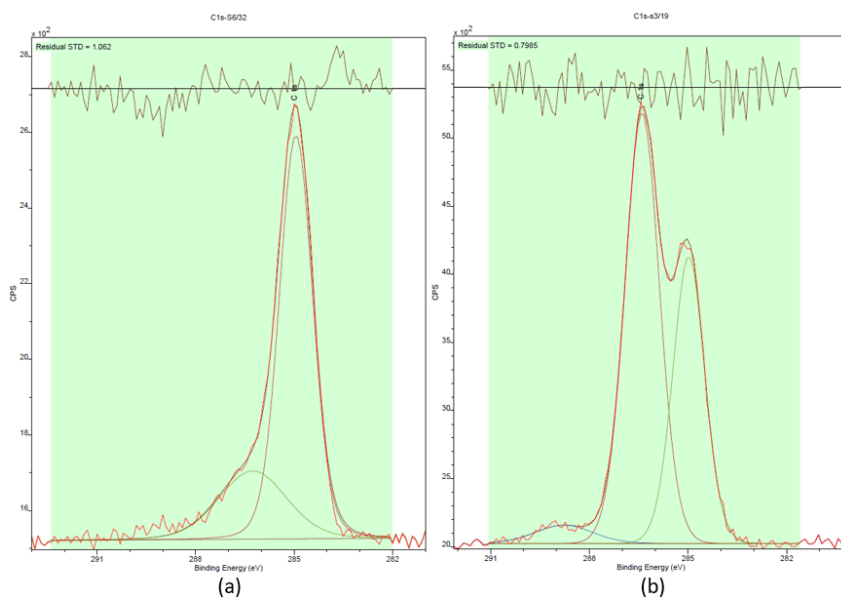


Figure 4.2.3- 1. XPS result of bare and PEO modified Au. C1s high resolution scan of bare and PEO-modified Au. (a) shows that high ratio of C-C component (285 eV) on the surface which may mainly come from dust and atmosphere contaminants. (b) C-O component (286.5 eV) largely increases and

C=O component (288.5 eV) both attribute to the fact that chemisorption of PEO is on the surface.

4.2.4 Mass spectroscopy:

The above results offer evidence that the surfaces are modified with PEO. Complex solution composed of a hundred of small metabolites was made for PEO layer incubation. Mass spectroscopy was used as an analysis tool scanning the PEO film modified on the golden surface to investigate the metabolites adsorption. The PEO surfaces were incubated with three different solvents, methanol, PBS, and acetonitrile, to extract the toxins adsorb on PEO films and the results are shown in Table 4.2.4-1. Mass analysis showed that there were 90 types of toxins detected in methanol, 57 types of toxins in PBS and 22 types of toxins in acetonitrile respectively. The undetected toxins may be due to three reasons, they did not adsorb onto the PEO layer, the amount of toxins adsorb was not enough to be detected by the system, and the toxins adsorbed but were not released during incubation. From the QCM-D experiments, it is obvious that PEO can reduce adsorption of small molecule. For the second reason, the concentration of these toxins may be diluted too much during incubation and lead to signal loss in the Mass machine. In addition, the difference in number of detected toxins between each solvent indicated that the small molecules have different affinity toward the solvents.

Table 4.2.4- 1 Different adsorption number of toxins by three solvents.

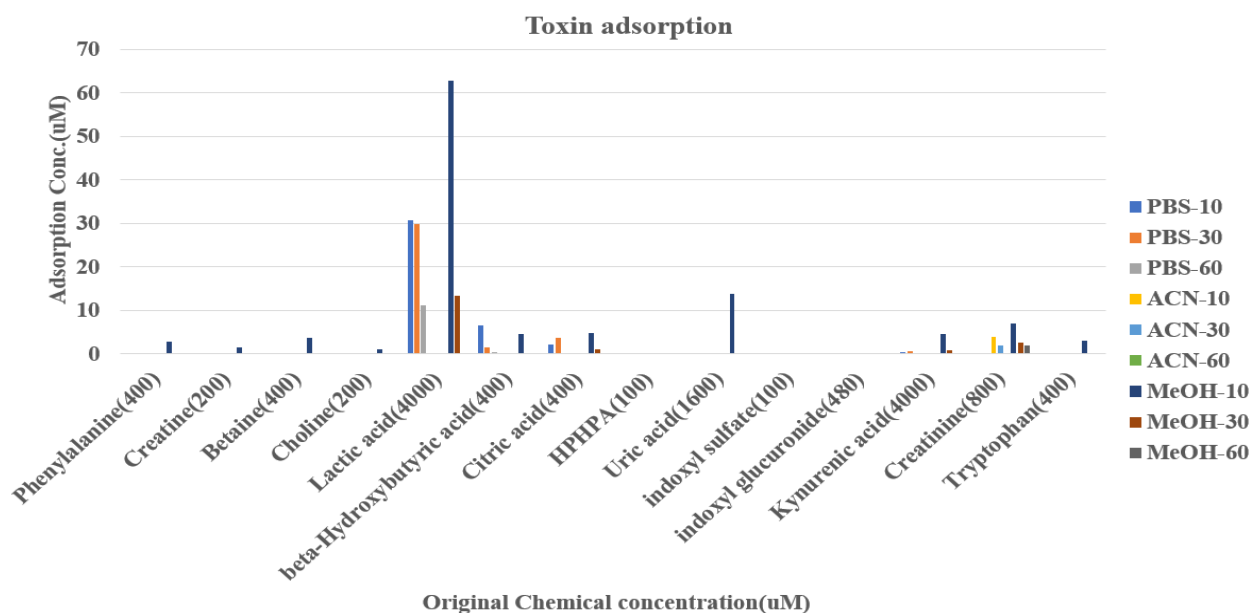
Extraction solvents	Adsorbed toxin species
Methanol	90
PBS	57
Acetonitrile	22

Besides of varied number for the solvents, the extraction results showed different tendencies for each incubation time. It is instinctive to understand that adsorption amount increases as increment of incubation time, however, which does not fit most adsorbed toxins. In contrast, decreased adsorption amount as incubation time fits more toxins. In addition, non-specific tendency is the third adsorption mode. As Table 4.2.4-2 showed, result of putrescine showed adsorption increased, adsorption of lactic acid decreased, and adsorption of leucine had no specific tendency as increment of incubation time. The latter two tendencies may be attributed to

competition and replacement between each toxin during incubation. Some adsorbed toxins may be replaced by other toxins with higher affinity and thus lead to small or non-specific adsorption amount tendency.

Table 4.2.4- 2 Three different adsorption tendencies during incubation with PBS extraction.

Sample	Putrescine (μM)	Lactic acid (μM)	Leucine (μM)
PBS (10 min)	0.196	30.7518916	1.13
PBS (30 min)	0.2	29.9416279	3.18
PBS-60 (1 hr)	0.237	11.0946973	2.81



Because there were a hundred toxins in the complex solution, it was not easy to figure out what properties of toxins affect their adsorption and replacement reaction. In addition, these metabolites may have interactions between each other [50]. To investigate the key factors of adsorption, we also compare the signal of most concentrated toxins and the toxins with lowest concentration in the complex solution as shown in Figure 4.2.4-1 and Figure 4.2.4-2. It is evident that the concentration of toxins in the complex solution do not directly correspond to adsorption of toxin and adsorption amount. In addition, putrescine is the only toxin extracted by PBS.

Figure 4.2.4- 1 The most concentrated toxins in complex solution. Kynurenic acid and uric acid have high concentration but do not have high adsorption amount.

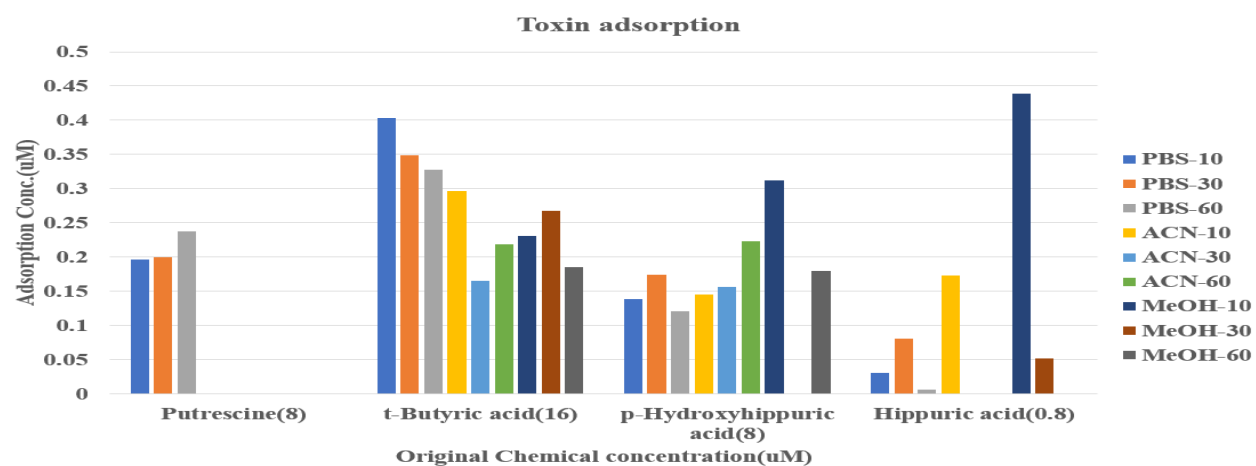


Figure 4.2.4- 2 The toxins with lowest concentration in the complex solution. The low concentration did not influence adsorption of these toxins. Moreover, putrescine was the only toxin extracted using PBS.

Besides, it should be noticed that isomer toxins had different adsorption amount as shown in Table 4.2.4-3. Adsorption amount of hydroxyproline differed with isomer and even the adsorption tendency was different. In contrast to hydroxyproline, isomer of leucine showed more apparent adsorption amount difference. Leucine was detected in PBS extraction for three incubation time while isoleucine was only detected in 10 minutes incubation which was very small compared to leucine. The result may imply isomers can be divided or distinguished through extraction from the polymer film.

Table 4.2.4- 3 Result of two different isomers extracted by PBS solvent.

Sample	cis-Hydroxyproline (μM)	trans-Hydroxyproline (μM)	Leucine (μM)	Isoleucine (μM)
PBS (10 min)	0.191	0.183	1.13	0.122
PBS (30 min)	0.169	0.15	3.18	< LOD
PBS (1 hr)	0.115	0.164	2.81	< LOD

On the other hand, the results showed physiological charge may play a role in adsorption by comparison of the most intense signal of toxins despite there were some exceptions. Furthermore, there were 14 species of toxins undetected in Mass results. Most of the undetected toxins are hydrophilic, acidic, small solubility in water and have aromatic structure. However, many adsorbed toxins also have similar properties, it needs further experiments to ensure the exact factors. Interestingly, IS was in the list while IS was proven to adsorb on PEO film in QCM-D experiment which also contributes to the idea that competition and replacement reaction between toxins.

Despite the Mass spectroscopy analysis was a preliminary experiment, we found that toxins may have different affinity to the extraction solvent, there may be replacement and competition between each toxin, the extraction process may have the ability to distinguish isomer of toxins, and physiological charge may play a role in adsorption part. Finally, it was proven that small metabolites adsorption on polymer film.

4.3 Protein adsorption results:

4.3.1 Dissipation of each experiment:

Dissipation can reflect the energy loss during the acoustic wave propagation. Furthermore, criterion of the validation of Sauerbrey equation relies on low dissipation and low $\Delta f_n/n$ between different overtones. The dissipation results are illustrated in Table 4.3.1-1. In all experimental conditions, the values of dissipation are similar and close to zero. Though values in the group of hydroxyl end-group PEO with IS and HSA introduction distributed from 5.21 to 7.16, they are still near to zero. In addition, $\Delta f_n/n$ curves for each overtone are low shown in Figure iii-2. Therefore, the Sauerbrey equation can be used for the analysis of the experimental data (eq. 2.1.4).

Table 4.3.1- 1 Dissipation data for experiments, average \pm SD ($n \geq 3$) at overtone = 3.

Surface	PEO type	D of PEO (E-6)	D of Small molecule (E-6)	D of HSA (E-6)
Bare Au + IS			0.12 ± 0.08	
Bare Au + HSA				3 ± 0.35
PEO + IS + HSA	HO-PEO	5.21 ± 0.57	5.91 ± 0.55	7.16 ± 0.72
PEO + IS + HSA	HO-PEO	Overnight (set at 0 after rinse)	0.035	2.42
PEO + skatole + HSA	CH ₃ -PEO	3.11 ± 1.5	3.36 ± 1.25	4.48 ± 1.26
PEO + skatole + HSA	CH ₃ -PEO	Overnight (set at 0 after rinse)	-0.15	1.13

4.3.2 HSA adsorption on Bare gold and PEO film:

HSA is a common protein used to study protein adsorption [13, 60, 64] and testing the anti-fouling ability of surfaces and is used herein as the standard protein for all QCM-D experiments. The adsorbed amount onto bare gold surface is tested and the frequency shift result yielded an adsorbed amount of 496 ± 49 ng/cm². HSA adsorption on PEO film is tested with two different end-groups on PEO: hydroxyl group and methoxy group. For investigation of the distal group effect on the anti-fouling ability after adsorption of IS. We first tested the adsorption amount of HSA on PEO film and the results of hydroxyl end-group PEO are shown in Table 4.3.2-1.

From Table 4.3.2-4, the HSA adsorption amount is largely decreased compared to data of adsorption on bare gold. The PEO adsorption was 915 ± 49 ng/cm² while the HSA adsorption was 255 ± 7.0 ng/cm². The result provides information that the PEO film resist the protein adsorption though the antifouling ability is not significant.

Table 4.3.2- 1 HSA protein adsorption on HO-PEO modified gold surface at overtone = 3.

Exp.	PEO type	PEO adsorption (ng/cm ²)	HSA adsorption (ng/cm ²)
Au + PEO + HSA	HO-PEO	880	260
Au + PEO + HSA		950	250
Au + PEO + HSA		overnight	30

Results for HSA adsorption on PEO with methoxy end-group were shown in Table 4.3.2-2. The amount of PEO adsorption was 285 ± 85 ng/cm² while the adsorption amount of HSA was 170 ± 28 ng/cm², Table 4.3.2-4. The PEO adsorption results are variable and lower than article record [36, 88], however, the PEO film still presented anti-fouling property to protein adsorption compared to data of adsorption on bare gold. Moreover, the PEO adsorption amounts were smaller than PEO with hydroxyl end-group. Though the PEO adsorption amount was smaller, the amount of HSA adsorption was smaller than hydroxyl end-group PEO.

Table 4.3.2- 2 HSA protein adsorption on CH₃-PEO modified gold surface at overtone = 3.

Exp.	PEO type	PEO adsorption (ng/cm ²)	HSA adsorption (ng/cm ²)
Au + PEO + HSA	CH ₃ -PEO	200	190
Au + PEO + HSA		370	150
Au + PEO + HSA		overnight	196.5

By comparison the adsorption plot of methoxy end-group and hydroxyl end-group PEO, hydroxyl end-group PEO showed unsatisfactory adsorption behavior which is shown in Figure 4.3.2-1. The slope of HO-PEO is large and does not achieve a plateau like methoxy end-group PEO does. This may indicate that HO-PEO-SH did not form a compact film on the surface and needed more time to achieve.

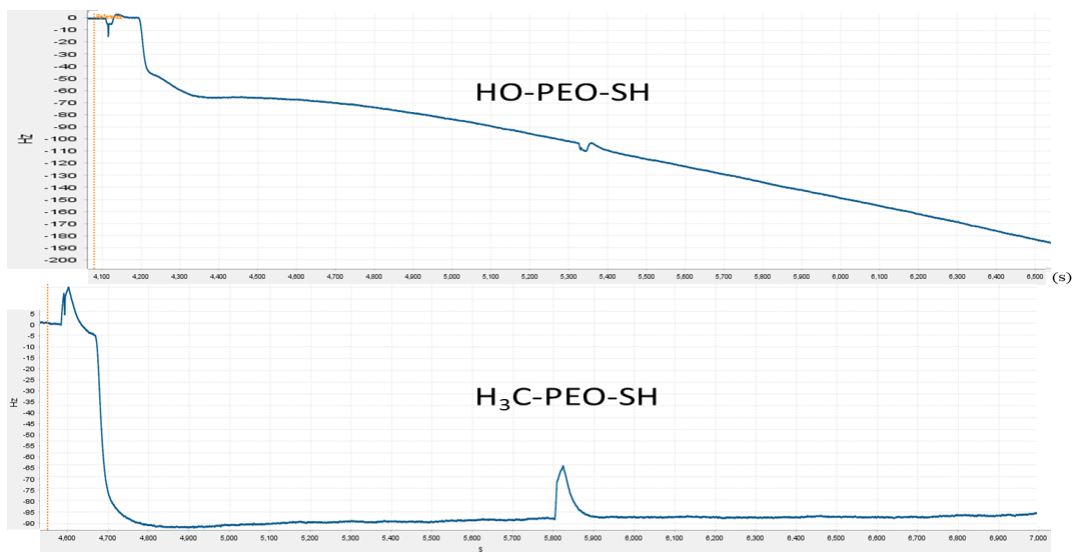


Figure 4.3.2- 1 Adsorption plot of HO-PEO and CH₃-PEO. The frequency shift of methoxy end-group PEO achieved plateau in 40 minutes while hydroxyl end-group PEO did not. (The blue line is frequency shift, and the orange line is baseline.)

To investigate this, the QCM sensor was incubated with hydroxyl end-group PEO solution overnight at 37°C. The result is shown in Figure 4.3.2-2. It is obvious that PEO adsorption line achieve plateau in 20 minutes. In addition, the HSA adsorption amount was reduced to 30.0 ng/cm² (Table 4.3.2-2). Comparison of bare gold and two types of PEO film is shown in Table 4.3.2-4.

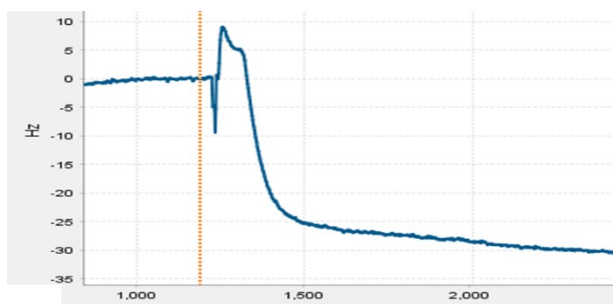


Figure 4.3.2- 2 Adsorption of HO-PEO after overnight incubation. The frequency shift of HO-PEO adsorption achieved plateau in 20 minutes after overnight incubation. (The blue line is frequency shift, and the orange line is baseline.)

Table 4.3.2- 3 HSA adsorption on bare gold and PEO modified surface. The data are average + SD ($n \geq 3$) at overtone = 3.

Sample	PEO type	PEO (ng/cm ²)	HSA (ng/cm ²)
Au + HSA			496.6 ± 49.07
PEO + HSA	HO-PEO	915 ± 49.49	255 ± 7.07
PEO + HSA	HO-PEO	Overnight	30.0
PEO + HSA	CH ₃ -PEO	285 ± 85.0	170 ± 28.28
PEO + HSA	CH ₃ -PEO	Overnight	196.5

From Table 4.3.2-3, the adsorption amount on bare gold is high compared with PEO modified surface. On the other hand, the surface may not be fully covered in HO-PEO which contributes to the relatively high protein adsorption [88]. In addition, HSA adsorption is varied with different end-groups which results from the covered extent of each PEO and/or the hydrophilicity difference between each end-group when protein molecules approach. For overnight experiment, the result may prove the hydroxyl end-group PEO film is more compact to repel protein adsorption than film grow in 40 minutes. In comparison, overnight incubation was also tested with CH₃-PEO, and the result showed that relatively high protein adsorption in CH₃-PEO case was not due to insufficient incubation time (Table 4.3.2-3).

4.3.3 Indoxyl sulfate (IS) adsorption on bare gold surface:

Adsorption of IS on bare gold was tested and the results are shown in Table 4.3.4-1. From the results, the IS adsorption was 36.2 ± 5.3 ng/cm² and which indicated that IS could adsorb onto bare gold without removing by PBS rinse. It is obvious the adsorption amount of IS decreased much due to the PEO film on the surface. In addition, the data of IS adsorption showed negative adsorption amount, thus high fundamental frequency (HFF) QCM-D was adopted for further investigation.

4.3.4 HSA adsorption on IS modified PEO surface:

From the results above, it can be concluded that the IS adsorption amount is affected by the PEO film significantly. HSA adsorption experiments after IS modification were done with two types of PEO, hydroxyl end-group and methoxy end-group. The results were summarized in Table 4.3.4-1. From the results, the adsorption amount of HO-PEO was $819.3 \pm 47.93 \text{ ng/cm}^2$ while the IS adsorption amount was $10 \pm 11.53 \text{ ng/cm}^2$, as the above section. In addition, the average of HSA adsorption ($11 \pm 11.75 \text{ ng/cm}^2$) was very small compared to the bare gold surface and even the virgin PEO film. This surprising result will be discussed later in section 4.3.7. For overnight incubation case, the HSA adsorption is higher than other groups. It is suggested that the space between each PEO chain of overnight incubation case is smaller and thus the adsorption of IS decreases. As a result of it, the 'inhibitor effect' from IS decreases (Table 4.3.4-1).

The results of methoxy end-group PEO are also shown in Table 4.3.4-1. The IS adsorption amount of methoxy end-group PEO is as small as the result of hydroxyl end-group PEO. Different from hydroxyl end-group PEO, PEO with methoxy end-group had lower adsorption amount of PEO and but higher adsorption of HSA. Importantly, the HSA adsorption seems not be affected by IS adsorption as much as the result of hydroxyl end-group PEO.

Binding of IS is highest on bare gold and reduced by PEO layer which is similar as protein adsorption (Table 4.3.4-1). This can be attributed to barrier established by PEO layer. In addition, it seems that IS binding were small in both types of PEO modified surface while IS adsorption amount is close to the detection limit of QCM-D for both types of PEO. Interestingly, results of HSA adsorption are quite different for PEO layer modified by IS in comparison with virgin PEO. HSA adsorption amount is higher for hydroxyl end-group PEO than methoxy end-group PEO except for the overnight incubation case. Moreover, HSA adsorption is lower for both types of PEO after IS modified which is decreased significantly hydroxyl end-group PEO from 255 ng/cm^2 to 11 ng/cm^2 . The result confirms the hypothesis that adsorption of small molecules influences the protein adsorption. IS behaved like an inhibitor in the experiments for hydroxyl end-group PEO. For methoxy end-group PEO, this phenomenon is not obvious which may be due to end-group property difference.

Table 4.3.4- 1 Adsorption of IS and HSA protein two types of PEO film. Data are presented as average + SD (n ≥ 3) at overtone = 3.

	PEO type	PEO (ng/cm ²)	IS (ng/cm ²)	HSA (ng/cm ²)
Au + IS			36.2 ± 5.3	
PEO + IS + HSA	HO-PEO	819.33 ± 47.93	10 ± 11.53	11 ± 11.75
PEO + IS + HSA	HO-PEO	Overnight	-11	72
PEO + IS + HSA	CH ₃ -PEO	297.5 ± 126.44	-12.25 ± 20.56	245.41 ± 91.58
PEO + IS + HSA	CH ₃ -PEO	Overnight	22	187

4.3.5 HSA adsorption on IS modified Hydroxyl end-group PEO film through HFF-QCM:

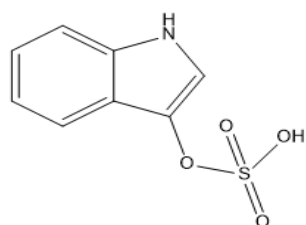
In low frequency QCM measurement, it seems IS modification effect is more significant on hydroxyl end-group PEO, however, the adsorption amount of IS on both of hydroxyl end-group and methoxy end-group are very small. Consequently, HFF-QCM was applied for better measurement resolution and further investigation of the IS adsorption amount and its effect on hydroxyl end-group PEO. Hydroxyl end-group PEO was used as target because its significant reduction of HSA adsorption. The results are shown in Table 4.3.5-1. PEO adsorption in HFF experiments were 210 and 140 ng/cm² respectively. IS adsorption amount was 17.5 ng/cm² and close to the results from low frequency QCM. HSA adsorptions were 16.5 ng/cm² for IS modified PEO film and 50 ng/cm² for virgin PEO film respectively. From the result, IS molecules were proved to adsorb onto PEO layer with small adsorption amount. On the other hand, interestingly, HSA adsorption on the IS modified PEO was also smaller than on the virgin PEO film. This may confirm the ‘inhibitor effect’ of IS adsorption to HSA adsorption.

Table 4.3.5- 1 HSA adsorption experiment with HFF-QCM.

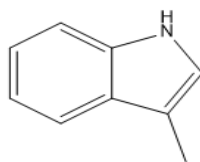
	PEO type	PEO (ng/cm ²)	IS (ng/cm ²)	HSA (ng/cm ²)
HFF-PEO + HSA	HO-PEO	140		50
HFF-PEO + IS + HSA	HO-PEO	210	17.5	16.5

4.3.6 HSA adsorption after small molecules modified thin films:

Based on the above experiments, the protein adsorption amount decreased after IS modified on PEO film and this effect was more significant on hydroxyl end-group PEO. The reason might be the negative charge of the IS molecules buried in the film. In order to investigate the reason, analogue of IS, skatole, was applied in further experiments. Skatole has similar chemical structure as IS but without charge (Figure 4.3.6-1).



Indoxyl sulfate



skatole

Figure 4.3.6- 1 Indoxyl sulfate and skatole. The sulfate group in indoxyl sulfate is replaced by methyl group in skatole.

Results of skatole adsorption experiments are shown in Table 4.3.6-1 while the comparison of IS adsorption is shown in Table 4.3.6-2. In Table 4.3.6-1, adsorption amount of skatole and HSA varies with adsorption amount of HO-PEO. Because the skatole adsorption was lower for higher PEO adsorption case, it is proposed that skatole can exclude the water inside PEO film. More water was excluded from higher adsorbed PEO film, as a result, the HSA adsorption was higher due to loss of hydration. It is noteworthy that skatole adsorption also decreased HSA adsorption in hydroxyl end-group PEO. In addition, the water exclusions behavior after introducing skatole molecules was only found in hydroxyl end-group PEO (Figure 4.3.6-2). On the other hand, IS cases showed lower HSA adsorption than skatole cases (Table 4.3.6-2). The results may indicate there is a ‘zwitterion-liked’ structure in the PEO film brought from IS adsorbed. However, this ‘zwitterion-liked’ structure may be weakened after overnight incubation because more compact hydroxyl end-group PEO film formed. Thus, HSA adsorption in overnight case did not decrease

as much as low-incubation time hydroxyl end-group PEO did. Besides, hydrophobic interaction between skatole molecule and PEO chains may contribute the lower HSA adsorption in hydroxyl end-group PEO case. In comparison, skatole was also applied in methoxy end-group PEO for testing. Unlike hydroxyl end-group PEO, the result showed that the HSA adsorption was not affected by skatole adsorption on the film (Table 4.3.6-2) which may be attributed to relatively compact structure of methoxy end-group PEO film (Figure 4.3.2-1).

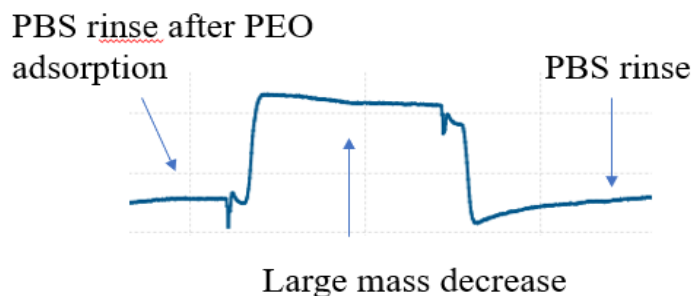


Figure 4.3.6- 2 Water exclusions by skatole molecule. This large frequency shift only shows up in HO-PEO experiments which may indicate the relatively strong interaction between skatole and HO-PEO chain.

Table 4.3.6- 1 Skatole and HSA adsorption on HO-PEO film at overtone = 3.

Exp.	PEO type	PEO (ng/cm ²)	Small molecule (ng/cm ²)	HSA (ng/cm ²)
PEO + skatole + HSA	HO-PEO	711.5	-3	20.25
PEO + skatole + HSA	HO-PEO	815.0	-15	58

4.3.7 Simple mechanism and conclusion:

PEO film was proved to reduce HSA and IS adsorption in our experiments. The mechanism of protein resistance was elaborated by many papers [38, 43, 89]. Though there were many different explanations, hydration state was relatively acceptable reason for the non-fouling ability of PEO. However, there were papers claimed that anti-fouling ability of PEO can breakdown by force or increased temperature [55, 56]. In contrast, our results showed that IS adsorption can be reduced by PEO film but further increase anti-fouling ability of PEO film. The inhibitor-like behavior of IS was confirmed again through HFF-QCM-D experiments. This result is similar as the paper

published by Peter et al, the binding of EGCg small molecules can decrease cell adhesion through hindering the binding site and increasing the rigidity of the polymer film [51]. In addition, nanoparticles modified by small molecules can also induce a different absorbing mode to the target cell reported by Prapainop et al. [49].

Table 4.3.6- 2 Adsorption of skatole and HSA on two types of PEO film at overtone = 3.

Exp.	PEO type	PEO (ng/cm ²)	Small molecule (ng/cm ²)	HSA (ng/cm ²)
PEO + IS + HSA	HO-PEO	819.33 ± 47.93	10 ± 11.53	11 ± 11.75
PEO + IS + HSA	HO-PEO	Overnight	-11	72
PEO + IS + HSA	CH ₃ -PEO	297.5 ± 126.44	-12.3 ± 20.6	245.4 ± 91.6
PEO + IS + HSA	CH ₃ -PEO	Overnight	22	187
PEO + skatole + HSA	HO-PEO	763.25 ± 51.75	-9 ± 8.5	39.1 ± 26.7
PEO + skatole + HSA	HO-PEO	Overnight	17	44
PEO + skatole + HSA	CH ₃ -PEO	258	8	231.5
PEO + skatole + HSA	CH ₃ -PEO	Overnight	-6	200

As our knowledge, buried charging IS molecules in PEO film may be the reason of this phenomena. The mixing molecules may express as polyelectrolytes because negative charge IS molecules adsorbed in the thin film and positive ions in PBS solution also absorbed into the film in order to neutralize the charge. These negative and positive charges may act as those ions in zwitterion polymer and thus enhance the hydrophilicity of the whole system.

As two-state theory mentions [56], the PEO film can be divided into hydrophobic and hydrophilic parts. The hydrophobic part is in the inner part of the film while the hydrophilic part

is the outer part. And the theory states that proteins are attracted by the inner part but repelled by the outer part. However, the multi-charged film structure may enhance the anti-fouling ability of both the inner and outer part and thus cause decreased HSA adsorption. Furthermore, the more hydrophobic inner part may be filled by nonpolar skatole and thus enhance the stability of the PEO chains. As a result, HSA molecules were repelled either by the complex charge structure caused from IS molecules or stronger hydrophobic interaction of the inner part of PEO film. The concept is shown in Figure 4.3.7-1. Importantly, either ‘zwitterion-liked’ structure or stronger hydrophobic interaction may be due to uncompact structure of PEO. Both effects are significantly strong in low incubation time hydroxyl end-group PEO case but very weak or even disappear in overnight incubation and methoxy end-group PEO case.

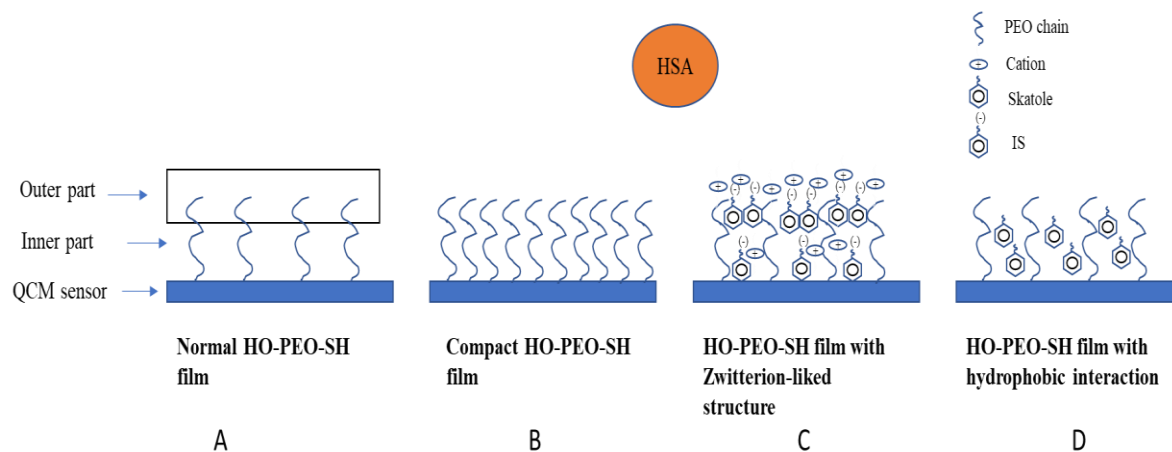


Figure 4.3.7- 1 Proposed mechanism of small molecules on PEO film. Based on two-state theory, four cases in our experiments were plotted. Case A shows the PEO film with smaller chain density that can attract proteins (HSA). Case B is the PEO film grow overnight, and which leads to more compact film with better antifouling ability. Case C is the PEO film with ‘zwitterion-liked’ structure due to IS adsorption, and which enhance the hydrophilicity of inner and outer part to repel proteins. Case D shows that the space between PEO chains filled with skatole molecules, and which leads to lower protein adsorption.

Though IS effect on PEO film was developed in our experiments, most of the uremic toxin effects remain unknown and undeveloped. In addition, our experiments and knowledge are not enough to give a comprehensive mechanism of inhibitor behavior of IS. Moreover, the corona of

the uremic toxin of CKD patients may lead to totally different result compared to individual small metabolite. The small metabolites and their effect on the anti-fouling polymers worth more attention and further investigation at future and which can definitely help us establish more holistic understanding and medical support of CKD.

5. Conclusion:

Thiolated-PEO with methoxy end-group was synthesis by esterification reaction and characterized by NMR. PEO film modified on gold surface was confirmed by QCM. The non-fouling ability of PEO film was shown by QCM through introduction of HSA protein to the PEO film. Interestingly, IS modified PEO film had better antifouling ability which may be due to the 'zwitterion-liked' structure. In addition, analogues of IS, i.e., skatole, were applied to further confirm the special interaction between small molecules and PEO chains. Despite lack of nonpolar properties, skatole experiment indicates hydrophobic interactions may also contribute to less protein adsorption result. Besides, QCM work proved that small molecules can be buried in PEO film instead of removal by PBS rinse.

PEO film on gold surface was further confirmed by XPS, water contact angle and ellipsometer. MS work results indicate that PEO film has the potential to be a way of storage to keep small uremic toxins. Methanol is the best solvent to extract these buried toxins from PEO film. Intriguingly, PEO film may be able to distinguish isomer chemicals. In addition, competitive adsorption and other interactions between each toxin was proved. Consequently, the adsorption amount of toxins does not increase as increment incubation time. Last but not the least, concentration of the toxins is not the main factor to affect adsorption amount.

6. Future work:

The effect of small molecule modification on protein adsorption on polymer film was first investigated in this work. Though only two molecules were applied, it was a good beginning in this field. The potential of PEO film as a material to capture or store uremic toxins in CKD patients' blood was also developed. The future work can be extended the PEO to other type of

polymer and investigation the interactions between the small molecules and the polymer. In addition, HSA can be changed to other proteins to figure out the influence of shape and charge difference. It is exciting to find different adsorption amount in PEO film between isomer chemicals. PEO as a promising antifouling material was proved to potentially have plentiful functions by combining with small molecules. The interactions between small molecules and polymers will be a profound step in medical field at future.

Reference:

1. Ziemba, C. et al. Antifouling Properties of a Self-Assembling Glutamic Acid-Lysine Zwitterionic Polymer Surface Coating. *Langmuir*, 2019. **35**(5): p. 1699-1713.
2. Wang, S.-Y.; Fang, L.-F.; Matsuyama, H. Construction of a stable zwitterionic layer on negatively-charged membrane via surface adsorption and cross-linking. *Journal of Membrane Science*, 2020. **597**: p. 117766.
3. Zheng, L. et al. Applications of zwitterionic polymers. *Reactive and Functional Polymers*, 2017. **118**: p. 51-61.
4. Sanchez-Cano, C.; Carril, M. Recent Developments in the Design of Non-Biofouling Coatings for Nanoparticles and Surfaces. *International Journal of Molecular Sciences*, 2020. **21**(3).
5. Bjoerling, M.; Karlstroem, G.; Linse, P. Conformational adaption of poly(ethylene oxide): A carbon-13 NMR study. *The Journal of Physical Chemistry*, 1991. **95**(17): p. 6706-6709.
6. Crupi, V. et al. Rayleigh wing and Fourier transform infrared studies of intermolecular and intramolecular hydrogen bonds in liquid ethylene glycol. *Molecular Physics*, 1995. **84**(4): p. 645-652.
7. Rundqvist, J.; Hoh, J.H.; Haviland, D.B. Poly(ethylene glycol) Self-Assembled Monolayer Island Growth. *Langmuir*, 2005. **21**(7): p. 2981-2987.
8. Jans, K. et al. Stability of Mixed PEO–Thiol SAMs for Biosensing Applications. *Langmuir*, 2008. **24**(8): p. 3949-3954.
9. Park, J. et al. Plasma-polymerized antifouling biochips for label-free measurement of protease activity in cell culture media. *Sensors and Actuators B: Chemical*, 2019. **281**: p. 527-534.
10. Zhong, J. et al. Counterion-Mediated Self-Assembly of Ion-Containing Block Copolymers on the Basis of the Hofmeister Series. *Macromolecular Chemistry and Physics*, 2019. **220**(5): p. 1800554.
11. Sharma, R.; Bahadur, P. Effect of different additives on the cloud point of a polyethylene oxide-polypropylene oxide-polyethylene oxide block copolymer in aqueous solution. *Journal of Surfactants and Detergents*, 2002. **5**(3): p. 263-268.

12. Yi, L. et al. New protein-resistant surfaces of amphiphilic graft copolymers containing hydrophilic poly(ethylene glycol) and low surface energy fluorosiloxane side-chains. *Applied Surface Science*, 2019. **480**: p. 923-933.
13. Bratek-Skicki, A. Design of Ultra-Thin PEO/PDMAEMA Polymer Coatings for Tunable Protein Adsorption. *Polymers*, 2020. **12**(3): p. 660.
14. Bratek-Skicki, A. et al. Reversible Protein Adsorption on Mixed PEO/PAA Polymer Brushes: Role of Ionic Strength and PEO Content. *Langmuir*, 2018. **34**(9): p. 3037-3048.
15. Morgese, G. et al. Mixing Poly(ethylene glycol) and Poly(2-alkyl-2-oxazoline)s Enhances Hydration and Viscoelasticity of Polymer Brushes and Determines Their Nanotribological and Antifouling Properties. *ACS Applied Materials & Interfaces*, 2018. **10**(48): p. 41839-41848.
16. Hespel, L. et al. Redox-Triggered Control of Cell Adhesion and Deadhesion on Poly(lysine)-g-poly(ethylene oxide) Adlayers. *ACS Applied Bio Materials*, 2019. **2**(10): p. 4367-4376.
17. Sun, X. et al. Antifouling Surfaces Based on Fluorine-Containing Asymmetric Polymer Brushes: Effect of Chain Length of Fluorinated Side Chain. *Langmuir*, 2019. **35**(5): p. 1235-1241.
18. Mumtaz, F. et al. Reversible Protein Adsorption on PMOXA/PAA Based Coatings: Role of PAA. *Chinese Journal of Polymer Science*, 2018. **36**(12): p. 1328-1341.
19. Baldim, V. et al. Monophosphonic versus Multiphosphonic Acid Based PEGylated Polymers for Functionalization and Stabilization of Metal (Ce, Fe, Ti, Al) Oxide Nanoparticles in Biological Media. *Advanced Materials Interfaces*, 2019. **6**(7): p. 1801814.
20. Gal, N. et al. Poly(ethylene glycol) Grafting of Nanoparticles Prevents Uptake by Cells and Transport Through Cell Barrier Layers Regardless of Shear Flow and Particle Size. *ACS Biomaterials Science & Engineering*, 2019. **5**(9): p. 4355-4365.
21. Zeuthen, C.M.; Shahrokhtash, A.; Sutherland, D.S. Nanoparticle Adsorption on Antifouling Polymer Brushes. *Langmuir*, 2019. **35**(46): p. 14879-14889.
22. Xu, B. et al. Biomimetic Asymmetric Polymer Brush Coatings Bearing Fencelike Conformation Exhibit Superior Protection and Antifouling Performance. *ACS Applied Materials & Interfaces*, 2020. **12**(1): p. 1588-1596.
23. Lv, J. et al. Effect of end-grafted PEG conformation on the hemocompatibility of poly(styrene-b-(ethylene-co-butylene)-b-styrene). *Journal of Biomaterials Science*, 2019. **30**(17): p. 1670-1685.

24. Kulka, M.W. et al. Mussel-Inspired Multivalent Linear Polyglycerol Coatings Outperform Monovalent Polyethylene Glycol Coatings in Antifouling Surface Properties. *ACS Applied Bio Materials*, 2019. **2**(12): p. 5749-5759.
25. Wanka, R. et al. Antifouling Properties of Dendritic Polyglycerols against Marine Macrofouling Organisms. *Langmuir*, 2019. **35**(50): p. 16568-16575.
26. Penna, M. et al. Hydration and Dynamics of Ligands Determine the Antifouling Capacity of Functionalized Surfaces. *The Journal of Physical Chemistry C*, 2019. **123**(50): p. 30360-30372.
27. Ngo, B.K.D. et al. Stability of silicones modified with PEO-silane amphiphiles: Impact of structure and concentration. *Polymer Degradation and Stability*, 2019. **163**: p. 136-142.
28. Sacchetti, C. et al. Surface Polyethylene Glycol Conformation Influences the Protein Corona of Polyethylene Glycol-Modified Single-Walled Carbon Nanotubes: Potential Implications on Biological Performance. *ACS Nano*, 2013. **7**(3): p. 1974-1989.
29. Shen, C. et al. Microstructure evolution of bonded water layer and morphology of grafting membrane with different polyethylene glycol length and their influence on permeability and anti-fouling capacity. *Journal of Membrane Science*, 2020. **601**: p. 117949.
30. Ma, C. et al. Graphene oxide-polyethylene glycol incorporated PVDF nanocomposite ultrafiltration membrane with enhanced hydrophilicity, permeability, and antifouling performance. *Chemosphere*, 2020. **253**: p. 126649.
31. Zhao, J. et al. Construction of Hemocompatible and Histocompatible Surface by Grafting Antithrombotic Peptide ACH11 and Hydrophilic PEG. *ACS Biomaterials Science & Engineering*, 2019. **5**(6): p. 2846-2857.
32. Szleifer, I. Protein adsorption on tethered polymer layers: effect of polymer chain architecture and composition. *Physica A: Statistical Mechanics and its Applications*, 1997. **244**(1): p. 370-388.
33. Pertsin, A.J.; Hayashi, T.; Grunze, M. Grand Canonical Monte Carlo Simulations of the Hydration Interaction between Oligo(ethylene glycol)-Terminated Alkanethiol Self-Assembled Monolayers. *The Journal of Physical Chemistry B*, 2002. **106**(47): p. 12274-12281.
34. Ren, C.L. et al. Molecular and Thermodynamic Factors Explain the Passivation Properties of Poly(ethylene glycol)-Coated Substrate Surfaces against Fluorophore-Labeled DNA Oligonucleotides. *Langmuir*, 2015. **31**(42): p. 11491-11501.

35. Hu, Y. et al. Study of fibrinogen adsorption on poly(ethylene glycol)-modified surfaces using a quartz crystal microbalance with dissipation and a dual polarization interferometry. *RSC Advances*, 2014. **4**(15): p. 7716-7724.
36. Ortiz, R.; Olsen, S.; Thormann, E. Salt-Induced Control of the Grafting Density in Poly(ethylene glycol) Brush Layers by a Grafting-to Approach. *Langmuir*, 2018. **34**(15): p. 4455-4464.
37. Al-Ani, A. et al. Tuning the Density of Poly(ethylene glycol) Chains to Control Mammalian Cell and Bacterial Attachment. *Polymers*, 2017. **9**(8): p. 343.
38. Dai, W. et al. A negative correlation between water content and protein adsorption on polymer brushes. *Journal of Materials Chemistry B*, 2019. **7**(13): p. 2162-2168.
39. Unsworth, L.D.; Sheardown, H.; Brash, J.L. Protein-resistant poly(ethylene oxide)-grafted surfaces: chain density-dependent multiple mechanisms of action. *Langmuir*, 2008. **24**(5): p. 1924-9.
40. Unsworth, L.D.; Sheardown, H.; Brash, J.L. Polyethylene oxide surfaces of variable chain density by chemisorption of PEO-thiol on gold: adsorption of proteins from plasma studied by radiolabelling and immunoblotting. *Biomaterials*, 2005. **26**(30): p. 5927-5933.
41. Unsworth, L.D.; Sheardown, H.; Brash, J.L. Protein Resistance of Surfaces Prepared by Sorption of End-Thiolated Poly(ethylene glycol) to Gold: Effect of Surface Chain Density. *Langmuir*, 2005. **21**(3): p. 1036-1041.
42. Tun, Z. et al. Determination of graft density of substrate-supported polymer films. *Physica B: Condensed Matter*, 2006. **385-386**: p. 697-699.
43. Unsworth, L.D. et al. Chemisorption of thiolated poly(ethylene oxide) to gold: surface chain densities measured by ellipsometry and neutron reflectometry. *Journal of Colloid and Interface Science*, 2005. **281**(1): p. 112-121.
44. Besseling, N.A.M. Theory of Hydration Forces between Surfaces. *Langmuir*, 1997. **13**(7): p. 2113-2122.
45. Ostuni, E. et al. Self-Assembled Monolayers That Resist the Adsorption of Proteins and the Adhesion of Bacterial and Mammalian Cells. *Langmuir*, 2001. **17**(20): p. 6336-6343.
46. Sofia, S.J.; Premnath, V.; Merrill, E.W. Poly(ethylene oxide) Grafted to Silicon Surfaces: Grafting Density and Protein Adsorption. *Macromolecules*, 1998. **31**(15): p. 5059-5070.

47. Chen, Y.; Luo, S.-C. Synergistic Effects of Ions and Surface Potentials on Antifouling Poly(3,4-ethylenedioxythiophene): Comparison of Oligo(Ethylene Glycol) and Phosphorylcholine. *Langmuir*, 2019. **35**(5): p. 1199-1210.
48. Chetwynd, A.J. et al. The Nanomaterial Metabolite Corona Determined Using a Quantitative Metabolomics Approach: A Pilot Study. *Small*, 2020. **16**(21): p. e2000295.
49. Prapainop, K.; Witter, D.P.; Wentworth, P. A Chemical Approach for Cell-Specific Targeting of Nanomaterials: Small-Molecule-Initiated Misfolding of Nanoparticle Corona Proteins. *Journal of the American Chemical Society*, 2012. **134**(9): p. 4100-4103.
50. Chetwynd, A.J.; Lynch, I. The rise of the nanomaterial metabolite corona, and emergence of the complete corona. *Environmental Science: Nano*, 2020. **7**(4): p. 1041-1060.
51. Peter, B. et al. Green tea polyphenol tailors cell adhesivity of RGD displaying surfaces: multicomponent models monitored optically. *Scientific Reports*, 2017. **7**(1): p. 42220.
52. Duranton, F. et al. Normal and pathologic concentrations of uremic toxins. *Journal of the American Society of Nephrology*, 2012. **23**(7): p. 1258-1270.
53. Leong, S.C.; Sirich, T.L. Indoxyl Sulfate-Review of Toxicity and Therapeutic Strategies. *Toxins*, 2016. **8**(12): p. 358.
54. Gryp, T. et al. p-Cresyl Sulfate. *Toxins*, 2017. **9**(2): p. 52.
55. Efremova, N.V.; Sheth, S.R.; Leckband, D.E. Protein-Induced Changes in Poly(ethylene glycol) Brushes: Molecular Weight and Temperature Dependence. *Langmuir*, 2001. **17**(24): p. 7628-7636.
56. Sheth, S.R.; Leckband, D. Measurements of attractive forces between proteins and end-grafted poly(ethylene glycol) chains. *Proceedings of the National Academy of Sciences*, 1997. **94**(16): p. 8399.
57. Tan, F. et al. Phase and mass relationship of the QCM sensor coated with rigid thin film. *International Conference on Communications, Circuits and Systems (ICCCAS)*. 2013.
58. Neupane, S. et al. Quartz Crystal Microbalance With Dissipation Monitoring: A Versatile Tool to Monitor Phase Transitions in Biomimetic Membranes. *Frontiers in Materials*, 2018. **5**(46).
59. Dixon, M.C. Quartz crystal microbalance with dissipation monitoring: enabling real-time characterization of biological materials and their interactions. *Journal of biomolecular techniques : JBT*, 2008. **19**(3): p. 151-158.

60. Kao, P. et al. Investigation of spontaneously adsorbed globular protein films using high-frequency bulk acoustic wave resonators. *SENSORS, 2010 IEEE*, 2010.
61. Stehrer, B.P. et al. High frequency QCM based sensor system for sensitive detection of dissolved analytes. *Procedia Engineering*, 2010. **5**: p. 835-837.
62. Cervera-Chiner, L. et al. High Fundamental Frequency Quartz Crystal Microbalance (HFF-QCM) immunosensor for pesticide detection in honey. *Food Control*, 2018. **92**: p. 1-6.
63. Mujahid, A.; Afzal, A.; Dickert, F.L. An Overview of High Frequency Acoustic Sensors—QCMs, SAWs and FBARs—Chemical and Biochemical Applications. *Sensors*, 2019. **19**(20).
64. Siow, K.S. et al. QCM-D and XPS study of protein adsorption on plasma polymers with sulfonate and phosphonate surface groups. *Colloids and Surfaces B: Biointerfaces*, 2019. **173**: p. 447-453.
65. Hampitak, P. et al. Protein interactions and conformations on graphene-based materials mapped using a quartz-crystal microbalance with dissipation monitoring (QCM-D). *Carbon*, 2020. **165**: p. 317-327.
66. Reviakine, I.; Johannsmann, D.; Richter, R.P. Hearing What You Cannot See and Visualizing What You Hear: Interpreting Quartz Crystal Microbalance Data from Solvated Interfaces. *Analytical Chemistry*, 2011. **83**(23): p. 8838-8848.
67. O’Sullivan, C.K.; Guilbault, G.G. Commercial quartz crystal microbalances – theory and applications. *Biosensors and Bioelectronics*, 1999. **14**(8): p. 663-670.
68. Montagut, Y.J. et al. Frequency-shift vs phase-shift characterization of in-liquid quartz crystal microbalance applications. *Review of Scientific Instruments*, 2011. **82**(6): p. 064702.
69. Alassi, A.; Benammar, M.; Brett, D. Quartz Crystal Microbalance Electronic Interfacing Systems: A Review. *Sensors*, 2017. **17**(12).
70. March, C. et al. High-frequency phase shift measurement greatly enhances the sensitivity of QCM immunosensors. *Biosensors and Bioelectronics*, 2015. **65**: p. 1-8.
71. Voinova, M.V. et al. Viscoelastic Acoustic Response of Layered Polymer Films at Fluid-Solid Interfaces: Continuum Mechanics Approach. *Physica Scripta*, 1999. **59**(5): p. 391-396.
72. Nalam, P.C. et al. Two-Fluid Model for the Interpretation of Quartz Crystal Microbalance Response: Tuning Properties of Polymer Brushes with Solvent Mixtures. *The Journal of Physical Chemistry C*, 2013. **117**(9): p. 4533-4543.

73. Du, B.; Johannsmann, D. Operation of the Quartz Crystal Microbalance in Liquids: Derivation of the Elastic Compliance of a Film from the Ratio of Bandwidth Shift and Frequency Shift. *Langmuir*, 2004. **20**(7): p. 2809-2812.
74. Alov, N.V. Fifty years of x-ray photoelectron spectroscopy. *Journal of Analytical Chemistry*, 2005. **60**(3): p. 297-300.
75. Crist, B.V. XPS in industry—Problems with binding energies in journals and binding energy databases. *Journal of Electron Spectroscopy and Related Phenomena*, 2019. **231**: p. 75-87.
76. Patel, D.I. et al. Introduction to near-ambient pressure x-ray photoelectron spectroscopy characterization of various materials. *Surface Science Spectra*, 2019. **26**(1): p. 016801.
77. Lefebvre, J. et al. Experimental methods in chemical engineering: X-ray photoelectron spectroscopy-XPS. *The Canadian Journal of Chemical Engineering*, 2019. **97**(10): p. 2588-2593.
78. Fadley, C.S. Atomic-level characterization of materials with core- and valence-level photoemission: basic phenomena and future directions. *Surface and Interface Analysis*, 2008. **40**(13): p. 1579-1605.
79. Ilyin, A.M. Chapter 11 - Auger Electron Spectroscopy, in *Microscopy Methods in Nanomaterials Characterization*, S. Thomas, et al., Editors. 2017, Elsevier. p. 363-381.
80. Hofer, F. et al. Fundamentals of electron energy-loss spectroscopy. *IOP Conference Series: Materials Science and Engineering*, 2016. **109**: p. 012007.
81. Ebnesajjad, S. Chapter 4 - Surface and Material Characterization Techniques, in *Surface Treatment of Materials for Adhesive Bonding (Second Edition)*, S. Ebnesajjad, Editor. 2014, William Andrew Publishing: Oxford. p. 39-75.
82. Ortega, R. et al. X-ray absorption spectroscopy of biological samples. A tutorial. *Journal of Analytical Atomic Spectrometry*, 2012. **27**(12): p. 2054-2065.
83. Hiroyuki, F. *Spectroscopic Ellipsometry: Principles and Applications*. 2003.
84. Tompkins, H.; J. Hilfiker. *Spectroscopic Ellipsometry: Practical Application to Thin Film Characterization*. 2015.
85. Lisboa, P. et al. Thiolated polyethylene oxide as a non-fouling element for nano-patterned bio-devices. *Applied Surface Science*, 2007. **253**(10): p. 4796-4804.

86. Du, Y.J.; Brash, J.L. Synthesis and characterization of thiol-terminated poly(ethylene oxide) for chemisorption to gold surface. *Journal of Applied Polymer Science*, 2003. **90**(2): p. 594-607.
87. Cuypers P.A. et al. The adsorption of prothrombin to phosphatidylserine multilayers quantitated by ellipsometry. *Journal of Biological Chemistry*, 1983. **258**(4): p. 2426-2431.
88. Delcroix, M.F.; Demoustier-Champagne, S.; Dupont-Gillain, C.C. Quartz Crystal Microbalance Study of Ionic Strength and pH-Dependent Polymer Conformation and Protein Adsorption/Desorption on PAA, PEO, and Mixed PEO/PAA Brushes. *Langmuir*, 2014. **30**(1): p. 268-277.
89. Binazadeh, M.; Kabiri, M.; Unsworth, L.D. Poly(ethylene glycol) and Poly(carboxy betaine) Based Nonfouling Architectures: Review and Current Efforts, in *Proteins at Interfaces III State of the Art*. 2012, American Chemical Society. p. 621-643.

Appendices:

i: PBS solution recipe

10x PBS solution was made by dissolving of 80 g sodium chloride (Sigma-Aldrich, USA), 2 g potassium chloride (Sigma-Aldrich, USA), 14.4 g disodium phosphate anhydrous (Scientific Fisher, USA), and 2.4 g potassium dihydrogen phosphate (Scientific Fisher, USA) in 1 L MilliQ water and 1x PBS was made by dilution of 10x PBS to ten times. All the salts used in making PBS solution were purchased from Sigma-Aldrich (USA). Both the solution can be stored under room temperature. It should be noted that pH value of 1x PBS and 10x PBS are different, around 7.4 and 6.9 respectively.

ii: Washing protocol for QCM sensors and small chips

Sensors and chips were first put under UV exposure to clean the surface for 5 minutes. Then, they were transferred into washing solution (Mixture of ammonia hydroxide (30% NH_4OH), hydrogen peroxide (30% H_2O_2) and MilliQ water was made at the volumetric ratio 1 : 1 : 5) at 75°C for 5 minutes. It is noted that sensors may float above the washing solution and thus decrease the efficiency of cleaning. To avoid such situation, a small glass stopper was put on the sensor. The surface was then rinsed with mixture solution of alcohol and MilliQ water at the volumetric ratio of 1 : 1. The surface were dried by inert gas and put under UV exposure for 5 minutes.

iii: QCM-D experiment

Sweep

Before the QCM-D experiment is begun, it is very important to run a sweep process. The sweep can give a first view and inspection of the condition of the sensor, shown in Figure iii-1. In Figure iii-1, susceptance and conductance are two parameters measured from calibration result of phase and amplitude voltage. With the figure of these two parameters, condition of the sensor can be clarified. A beginning sweep was run without changing

anything for looking for the correct parameters. The middle point between two extrema of plot A was set to be the new central frequency. It is recommended to choose parameter A as reference instead of parameter B which has more misunderstanding noise peaks. The points and span were set to be 1000 and 5.0 kHz respectively while value of step would be automatically set to 5.0 Hz after the above two numbers were set. Normally, the shape should be clean, flat, and symmetrical like Figure iii-1. In addition, the intensity of plot a should be higher than 10 in air or the sensor may be contaminated, damaged or misplaced.

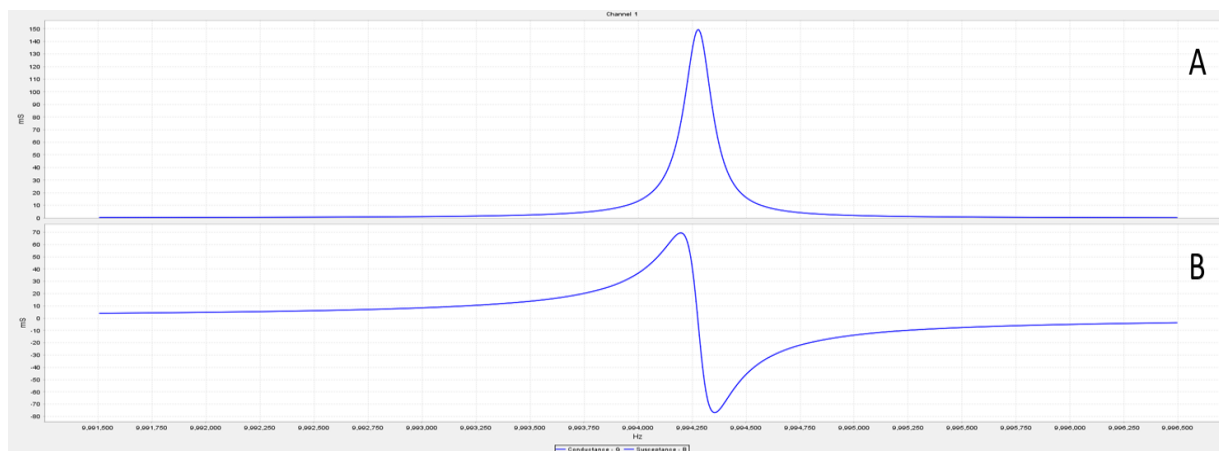


Figure iii- 1 Sweeping result of the sensor. The plot can give a brief view of the condition of the sensor.

Disturbance

The flowrate of the QCM experiment was controlled by QSD-FCU. The maximum volume of flow per time is largely limited to the volume of the syringe mounted in the FCU. QCM is an equipment used to measure the loading on the sensor, it is inherited that signal would be different during transition of the syringe, shown in Figure iii-2. In Figure iii-2, it is clear that a noise-liked peak showed up in both frequency shift and dissipation change regularly. This disturbance signal does not influence the result of experiment but affect reading. To decrease showing frequency of the disturbance, it is suggested either increase the volume of the syringe or decrease the flowrate. In addition, the minimum flowrate is fixed with the volume of syringe, i.e., 5% of the maximum volume of the syringe per minute.

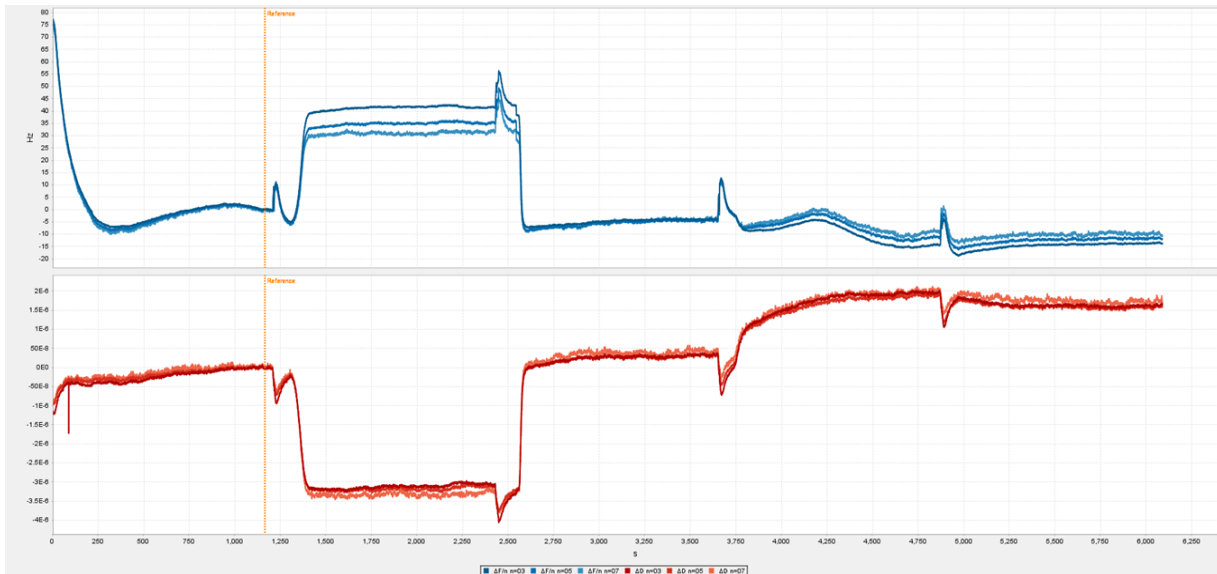


Figure iii- 2 Disturbance signal in an experiment. Orange dash line was the baseline, blue line was the frequency shift and red line represent the dissipation change. The experiment is introduction of HSA into skatole-modified PEO film. The experiment condition was under 37 °C and flowrate was fixed at 50 ul/min. It is clear that disturbance signal showed up regularly.

On the other hand, the strength and length of the disturbance are affected by the flowrate strongly. The strength of the disturbance peak was enhanced after the flowrate was double, shown in Figure iii-3. The length of the disturbance signal highly depends on the flowrate of ejection. The higher the flowrate of ejection, the shorter the length will be, cases do not show here.

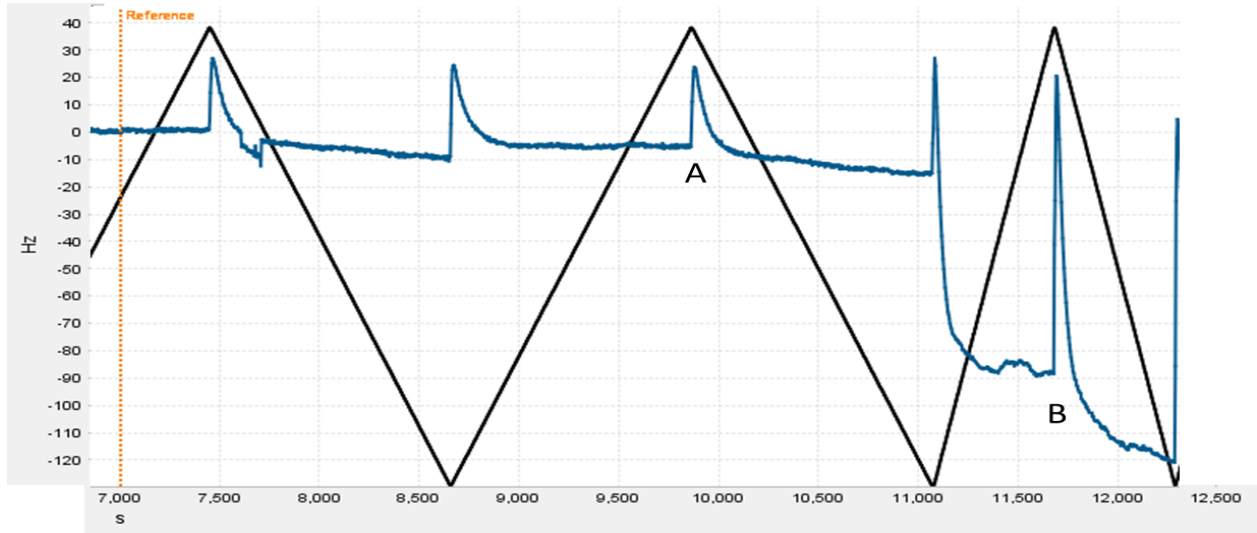


Figure iii- 3 The different disturbance signal reflected from different flowrate. The orange dash line was baseline, the black line is the syringe loaded volume and the blue line represented the frequency shift. It is apparent that the disturbance peak B was times higher than peak A when the flowrate was double near 11000s.

Detail of QCM experiment

Before QCM-D experiment, the main solvent, PBS solution, should be degassed to avoid bubbles generating in the cell when running experiments. The PBS solution was heated up to 40 °C and connected with a Y-shaped tube and the other side of the tube was connected with MilliQ water in case there is evaporation during degassing. And the above combination should be put into a sonicate machine for temperature control and sonication. It is noteworthy that the degassing solution should not directly be connected to the pump, instead, there was a water trap set by molecular sieves between the pump and the degassing solution to avoid breaking pump due to enter of water. Before and after the degassing, volume of the PBS should be measured to ensure the salt concentration is consistent. If the volume is smaller, addition of degas MilliQ water should be done. All the experimental solutions were transferred into test tubes wrapped with small amount of cotton and a small piece of aluminum foil to reduce the temperature difference between solution and the QCM cell. The test tubes were placed in temperature control in front of the cell and capped with silicone stoppers and a small piece of paraffin to avoid dust contamination and evaporation. It should be noticed that the flow tube connects the cell and solution should be as shorter as possible to reduce the heat loss during solution transportation. Moreover, the flow tube between the cell and test tube was cleaned by MilliQ water before put into the test tube to remove the dust.

The experiments were run under 37 °C and flowrate was set to be 50 and 1500 ul/min for injection and disposal respectively. There were bumps showing up for a period of time because of the limited volume of syringe. To decrease amplitude of the bump and reduce its numbers, the injection rate was set to be small and the disposal rate was set to be times bigger than injection rate. It should be noted that temperature was set to 37°C for at least 30 minutes before measurement and solution injection in order to stabilize the signal because QCM-D signal is very sensitive to temperature difference and which can decrease production of bubbles during experiment. The working mode of the experiment was set to high-resolution mode and data

average was set to 20 due to better stability and quality of long-term measurement. PBS solution was injected into the cell for 1 hr before the next addition of chemicals due to stability of signal under wet measurement. Flow was begun after 1 hr and the baseline (Δf_0) was set when Δf is stable under PBS flow. Δf and ΔD are recorded after every rinse for calculating to the surface density of each chemical and analyzing the surface properties of the PEO thin film. After the baseline was set, PEO injection was begun for around 40 minutes until the signal arrived plateau and then followed by PBS rinse about one hour, depends on signal stability, to get Δf_1 which represented the mass amount of PEO adsorption on the surface. Indoxyl sulfate solution was injected for 20 minutes after PBS rinse and followed by PBS rinse again for 20 minutes. HSA solution was injected for 20 minutes after the rinse. PBS rinse was conducted after HSA injection to get Δf_3 which gave HSA adsorption amount.

iv: Gold coating chips

Gold coating chips were made from 150 mm silicon wafer with boron doped and (1,1,1) orientation. The blank wafer was washed by piranha solution for 15 minutes in cleanroom to get rid of surface contamination and dried by nitrogen flow. The wafer was then coated with 6 nm Cr as an adhesive layer and followed by 6 nm Au coating. Before dicing, the thickness of coatings of the wafer were analyzed by ellipsometer from $60^\circ \sim 75^\circ$. The wafer was then diced into $0.5 \times 0.5 \text{ cm}^2$ small chips.

v: Uremic toxin adsorption experiment on small chips

The small Au-coated chips from appendix iv were washed with cleaning protocol from appendix ii, transferred into 5 mM PEO solution and incubated overnight at room temperature. The chips were rinsed with PBS solution and put into centrifuge tubes filled with uremic solution at 37°C for three different time periods, 10 minutes, 30 minutes and 1 hour. Chips were analyzed by ellipsometer, XPS and water contact angle before and after PEO modification. For each time point, solution rest on the chip surface was removed through touching the edge of the chips to corresponding incubation solution, that is toxin solution. It should be noted that a thin water film on the surface is acceptable because of the hydrophilicity of PEO film. After drying process, for each time point, the chips were incubated in methanol at 37°C overnight. It was noteworthy that

volume of incubation solvent should be controlled as lower as possible because dilution of the toxins may cause signal loss during LC-MS analysis.